Molecular basis of ALK1-mediated signalling by BMP9/BMP10 and their prodomain-bound forms

Richard M Salmon[1,#], Jingxu Guo[1,#], Jennifer H Wood[1], Zhen Tong[1], John S Beech[2], Aleksandra Lawera[1], Minmin Yu[3], David J Grainger[2], Jill Reckless[2], Nicholas W Morrell[1], Wei Li[1,*]

1. The Department of Medicine, University of Cambridge School of Clinical Medicine, Cambridge, CB2 0QQ, United Kingdom; 2 RxCelerate Ltd, Babraham Research Campus, Cambridge, CB22 3AT, United Kingdom; 3. MRC Laboratory of Molecular Biology, Francis Crick Avenue, Cambridge CB2 0QH, United Kingdom;

Running title: Molecular basis of ALK1 signalling

 # These authors contributed equally

**** Corresponding Author:***

Dr Wei Li

Department of Medicine, University of Cambridge

Level 5, Addenbrooke's Hospital

Box 157, Hills Road, Cambridge, CB2 0QQ

Email: wl225@cam.ac.uk

Tel.: +44 (0) 1223 761304

Fax: +44 (0) 1223 336846

Abbreviations

ActRIIa/b, Activin type II receptor a/b; ALK1 (2,3&6), Activin receptor-like kinase 1 (2,3&6); ALK1-Fc, ALK1 extracellular domain-Fc fusion protein; ALP, Alkaline phosphatase; BMP, Bone morphogenetic protein; BMPR2, BMP receptor type II; CV2, Crossveinless 2; ECD, Extracellular domain; ENG, Endoglin; GDF5, Growth differentiation factor 5; GF, Growth factor; HHT,

Hereditary haemorrhagic telangiectasia; H-bond, hydrogen bond; HO, Heterotopic ossification; ID1, Inhibitor of DNA binding protein 1; PAECs, Pulmonary artery endothelial cells; PAH, Pulmonary arterial hypertension; PASMCs, Pulmonary artery smooth muscle cells; proBMP9(10), Unprocessed proBMP9(10); Pro-BMP9(10), Furin-processed complex containing the prodomain non-covalently bound to the GF-domain of BMP9(10); QF, quadriceps femoris; RMSD, root-mean-square deviation; sENG, soluble endoglin; SPR, surface plasmon resonance; TGFβ, Transforming growth factor β; WT, wild type.

Abstract

Activin receptor-like kinase 1 (ALK1)-mediated endothelial cell signalling in response to bone morphogenetic protein 9 (BMP9) and BMP10 is of significant importance in cardiovascular disease and cancer. However, detailed molecular mechanisms of ALK1-mediated signalling remain unclear. Here, we report crystal structures of the BMP10:ALK1 complex at 2.3 Å and the prodomain-bound BMP9:ALK1 complex at 3.3 Å. Structural analyses reveal a tripartite recognition mechanism that defines BMP9 and BMP10 specificity for ALK1, and predict that crossveinless 2 is not an inhibitor of BMP9, which is confirmed by experimental evidence. Validating the tripartite mechanism by introducing BMP10-specific residues into BMP9 has generated BMP10-like ligands with diminished signalling activity in C2C12 cells. Surprisingly, the loss of osteogenic signalling in C2C12 does not translate into non-osteogenic activity *in vivo* and BMP10 also induces bone-formation. Collectively, these comprehensive data provide essential insight into ALK1-mediated BMP9 and BMP10 signalling, facilitating therapeutic targeting of this important pathway.

Keywords: BMP9, BMP10, ALK1, specificity, crystal structure

Introduction

Bone morphogenetic proteins (BMPs) are dimeric transforming growth factor β (TGFβ) family cytokines, initiating cellular signalling by forming a complex with two copies of type I receptors and two copies of type II receptors, both of which are type I transmembrane proteins with an intracellular serine/threonine kinase domain. Activin receptor-like kinase 1 (ALK1) is a type I receptor specifically expressed on endothelial cells [1], mediating the signals from BMP9 and BMP10 exclusively [2]. BMP signalling can be regulated by co-receptors, such as endoglin (ENG), as well as extracellular ligand traps, such as noggin and crossveinless 2 (CV2) [3]. All TGFβ family ligands are synthesised as preproproteins, processed by furin-like proprotein convertase upon secretion. It has been shown for several family members, including TGFβ, BMP9 and BMP10, that the prodomain remains tightly bound to the growth factor (GF) domain in circulation [4-6]. Hence, the prodomain may also contribute to the regulation of BMP signalling. BMP9 and BMP10 share a high degree of sequence identity (64% in the GF-domain and 33% in the prodomain); both ligands induce similar target genes in endothelial cells [7] and BMP10 is able to compensate for the function of BMP9 in *Bmp9* knockout mice [7,8]. Compared with other BMPs, BMP9 and BMP10 possess several unique features. Firstly, both ligands bind to ALK1 and ENG with sub-nanomolar affinities [9,10]; and the affinities of both ligands for their cognate type I receptor ALK1 (EC_{50} of around 50 pg ml^{-1}) are much higher than those of other BMPs for their cognate type I receptors ALK2, ALK3 and ALK6 (EC_{50} of around 50 ng ml^{-1}) [4]. Secondly, whilst several naturally-occurring extracellular ligand traps have been described for BMPs, most of them do not inhibit BMP9 or BMP10 signalling [3], apart from reports that CV2 binds to BMP9 and BMP10 and suppresses their signalling [11,12].

ALK1-mediated endothelial BMP9 and BMP10 signalling plays many important roles in angiogenesis and the maintenance of vascular quiescence [13,14]. Defects in this pathway are known to cause cardiovascular diseases. For instance, individuals with heterozygous loss-of-

function mutations in *ALK1* or *ENG* develop hereditary haemorrhagic telangiectasia (HHT) [15,16], and *BMP9* mutations have been identified in patients with a phenotype similar to HHT [17]. Typical HHT manifestations involve vascular abnormalities such as arteriovenous malformations in the brain, lung, liver or gastrointestinal tract. In addition, heterozygous loss-of-function mutations in the type II BMP receptor *BMPR2*, as well as in *ALK1*, *ENG* and *BMP9*, have been identified in patients with pulmonary arterial hypertension (PAH) [18-21]. The pathophysiology of PAH includes endothelial dysfunction and vascular remodelling, resulting in narrowing of pulmonary arteries, elevated pulmonary arterial pressure and right ventricular heart failure [22]. Importantly, targeting the endothelial BMP pathway has promising therapeutic potential. For example, administration of recombinant BMP9 prevented and reversed the disease and inhibited angiogenesis in preclinical PAH models [23]. Moreover, ALK1-Fc (Dalantercept) and an anti-ENG antibody (TRC105) have demonstrated anti-tumour angiogenesis activity and are currently in phase II clinical trials for treating selected solid tumours [24-26].

A comprehensive understanding of the molecular mechanisms behind BMP9 and BMP10 signalling will provide important information for translating therapies that target the endothelial BMP pathway. There are a number of questions that remain to be answered, particularly regarding the difference between BMP9 and BMP10 as well as the regulatory role of the prodomain. Although BMP9 and BMP10 have been shown to induce several identical genes in endothelial cells [7], no direct comparison of the global transcription regulated by these two ligands has been performed to date, especially by their circulating prodomain-bound forms (pro-BMP9 and pro-BMP10, see Supplementary Fig 1). In addition, despite several crystal structures of BMP9 being solved, either as GF-domain alone or GF-domain in complex with receptors, the co-receptor or the prodomain [9,27-30], crystal structures of BMP10 remain to be elucidated.

In this study, we directly compare global gene expression regulated by the circulating forms of pro-BMP9 and pro-BMP10 using microarray. We report the crystal structures of BMP10 GF-domain in complex with ALK1 to 2.3 Å and prodomain-bound BMP9 in complex with ALK1 to 3.3 Å. Structural and sequence analyses alongside previously reported BMP9 structures [9,29,30] enable the identification of two conserved regions in BMP9 and BMP10 that define their specificity for ALK1, ENG and their prodomains. Furthermore, our structural analysis suggests CV2 does not inhibit BMP9 signalling, which we confirm here by experimental evidence, in contrast to a previous report [11]. Finally, guided by the structural analysis, we have successfully modified BMP9 signalling specificity by single amino acid substitutions. Surprisingly, we find that *in vitro* alkaline phosphatase (ALP)-based osteogenic signalling activity does not correlate with *in vivo* heterotopic ossification and that previously reported non-osteogenic BMP10 can induce bone formation *in vivo*.

Results:

Pro-BMP9 and pro-BMP10 are equivalent ALK1 ligands

Although pro-BMP9 and pro-BMP10 are the *in vivo* circulating forms of ligands [4,5], most of the previous signalling and functional studies on BMP9 and BMP10 have employed the GF-domain alone. Thus, it is essential to establish whether pro-BMP9 and pro-BMP10 bind to ALK1 and signal in endothelial cells in the same manner as their GF-domains. We first compared whether pro-BMP9 and pro-BMP10 can signal with similar potency to their GF-domains. As shown in Figure 1a, in a dose-response assay in human pulmonary artery endothelial cells (PAECs) using *ID1* gene induction as a readout, pro-BMP9 and pro-BMP10 exhibited identical potency to BMP9 and BMP10 GF-domains, respectively.

We then carried out a microarray experiment to establish whether there is any differential gene induction by pro-BMP9 and pro-BMP10 in endothelial cells. As shown in Figure 1b-d and Supplementary Data 1 and 2, both pro-BMP9 and pro-BMP10 induced and suppressed similar transcript expression when compared with PBS-treated controls; indeed, there was no significant difference in gene induction or suppression when comparing pro-BMP9 with pro-BMP10, providing evidence that they are functionally equivalent ALK1 ligands *in vitro* on endothelial cells. We further compared the ALK1 binding affinity of pro-BMP9 and pro-BMP10 to that of BMP9 and BMP10, respectively, using Surface Plasmon Resonance (SPR). As shown in Figure 1e&f, the K_D values measured for BMP9:ALK1-Fc and BMP10:ALK1-Fc (48.1 pM and 34.3 pM, respectively) were very similar to those previously reported (45.22 pM and 10.3 pM, respectively) [9]. In addition, both BMP9 and BMP10 bound to the ALK1 monomer (produced in house)[28] and dimer (ALK1-Fc) with similar affinities, irrespective of the presence of their prodomains (Fig 1e&f), which supported the findings from Figure 1a that the prodomain does not interfere with ALK1-mediated signalling potency.

Structure of BMP10:ALK1 complex

To delineate the molecular details of ALK1-mediated BMP10 signalling, we solved the crystal structure of the BMP10 GF-domain in complex with the ALK1 extracellular domain (ECD) to 2.3 Å (Fig 2a, Supplementary Table 1, Supplementary Fig 2&3). As expected, the ALK1 ECD binds BMP10 in a 2:2 stoichiometry, and the two ALK1 ECD monomers are not in direct contact. The assembly of BMP10:ALK1 is identical to that of BMP9:ALK1 in the BMP9:ALK1:ActRIIb complex (PDB:4FAO), with mainchain root-mean-square deviation (RMSD) of 0.84 Å for BMP dimer, 0.52 Å for ALK1 monomer. The total buried surface area of the BMP10:ALK1 interface is slightly smaller than that of the BMP9:ALK1 interface (Fig 2b), however, the percentage of contribution from the two monomers is similar. Importantly, the ALK1 binding sites on BMP9 and BMP10 are mostly conserved, which corresponds well with the above data that these ligands bind ALK1 with comparable affinity and stimulate ALK1-dependent signalling in endothelial cells with similar potency.

Specificity determinants in the BMP9 and BMP10 subfamily

The high affinity of BMP9 and BMP10 for ALK1 and their specificity for ALK1-mediated signalling suggest that these ligands possess common specificity determinants. The crystal structure of the BMP10:ALK1 complex, alongside the previously reported complex structures of BMP9 [9,29,30], provide a unique opportunity to identify such specificity determinants.

Most BMPs have higher affinities for the type I receptors, such as BMP2 and BMP4 for ALK3, BMP9 and BMP10 for ALK1, and BMP14 (also called GDF5) for ALK6. The exceptions are BMP6 and BMP7, which signal via ALK2 but bind to the type II receptors ActRIIa and ActRIIb with higher affinity. Among the four type I receptors that are known to mediate BMP signalling, the high affinity ligands for ALK1, ALK3 and ALK6 have been described and crystal structures of

these receptors bound to their cognate ligands been solved [9,31,32], whereas the existence of high affinity ligand(s) for ALK2 is yet to be confirmed.

A close examination of sequence alignment between the five representative BMPs with high affinities for the type I receptors as well as BMP6 and BMP7 revealed a total of 16 residues that are preferentially conserved between BMP9 and BMP10 (Fig 3a, highlighted in cyan, blue and yellow). Interestingly, these residues can be mapped onto three regions of BMP10 (Fig 3b&c), the type I receptor-binding site, the type II receptor-binding site and the middle of the BMP dimer interface.

The type I receptor binding site and conserved region 1

Using the PDBePISA server[33], a total of 26 BMP10 residues were identified at the ALK1 binding interface (Fig 3a, lines over the sequence). Interestingly, these residues can be divided into three groups (Fig 4a): those conserved across different subgroups of BMPs (in red, also * over the top of the sequence in Fig 3a), those conserved only among BMP9 and BMP10 (in cyan, referred to as conserved region 1) and those that vary between BMP9 and BMP10 (in yellow). The interactions between BMP10 and ALK1 cover the same three sites as previously identified between BMP9 and ALK1 in the 3.35 Å BMP9:ALK1:ActRIIb structure[9], but the 2.3 Å resolution reveals the BMP10:ALK1 interface in more detail (Fig 4b-f). Sites II and III within the type I receptor binding area, which have been proposed to hold the key to ALK1 specificity for BMP9 [9], indeed harbour the residues unique to BMP9 and BMP10 (Fig 4c&d, cyan). At the site II, ALK1-specificity is defined by a hydrogen bond (H-bond) between BMP10 S339 and the mainchain oxygen of ALK1 R78, and a salt bridge between BMP10 D338 and ALK1 R80. Site III contains two residues conserved between BMP9 and BMP10 that contribute to the ALK1 specificity, but they differ in molecular interactions in the two complexes. While ALK1 H73 forms a H-bond with BMP10 P366, ALK1 E75 forms a H-bond with Y413 which is conserved

192 across all BMPs. Overlaying the BMP2:ALK3 structure[31] revealed that although the equivalent
193 residue Y385 in BMP2 makes a similar H-bond with ALK3 D84, there is a significant movement
194 in BMP10 mainchain conformation due to the unique insertion of F411 (and Y416 in BMP9, Fig
195 3a). Thus K368, the BMP9 and BMP10-specific residue, defines the ALK1 specificity by
196 interacting with the mainchain oxygen on the BMP10 loop, allowing Y413 to be in close
197 proximity for interacting with ALK1. Reciprocally, ALK1 evolved a negatively charged residue
198 with a longer side-chain at the corresponding position, E75, to allow the H-bond formation
199 with Y413, defining its specificity for BMP9 and BMP10. The site I region contains residues that
200 are different between BMP9 and BMP10, with the interactions predominantly mediated by
201 sidechains (Fig 4e). In contrast, the core of the interface is conserved across all BMPs and
202 mostly hydrophobic in nature (Fig 4f). From the ALK1 side, residues H73, E75, R78 and R80
203 interact with amino acids that are unique to BMP9 and BMP10 hence define the ALK1
204 specificity (Fig 4c&d). Interestingly, these ALK1 residues are located near or within the two
205 loops of ALK1 that have significantly different conformation from those loops in ALK3 and
206 ALK6 due to a 2-3 amino acid deletions (Fig 4g&h, Supplementary Fig 4). Therefore, ALK1
207 specificity is maximised through the presence of specific residues and through their unique
208 display by shortening the length of the loops on which these residues are positioned.
209
210 **The type II receptor binding site and conserved region 2**
211 Of the BMP type II receptors, the structures for ActRIIa:BMP7 (PDB:1LX5)[34], ActRIIa:BMP2
212 (PDB:2GOO)[31], ActRIIb:BMP2 (PDB:2H62)[35] and ActRIIb:BMP9 (PDB:4FAO)[9] have been solved.
213 Analysis of the ActRIIb binding site on BMP9 revealed that 26 residues contributed
214 significantly to the receptor-binding interface (Fig 3a, lines below the sequences). Similar to
215 the type I receptor-binding site, a subset of these residues, again mostly hydrophobic, are
216 highly conserved across different BMPs (Fig 3a, * below the sequences) and can be mapped to

217 the centre of the type II surface on BMP9 (Fig 5a, red). The variable residues, specifically those
218 residues that differ between various BMP ligands (Fig 5a, yellow), as well as the conserved
219 region 2 residues that are conserved in BMP9 and BMP10 alone (Fig 5a, blue), surround these
220 conserved residues. When comparing the electrostatic surface, the ActRIIb binding site on
221 BMP9 is mostly conserved in BMP10 (Fig 5b), consistent with a previous report that both
222 ligands bind ActRIIb with similar affinities [9].
223 The most striking feature in the conserved region 2 is the insertion of a hydrophobic residue,
224 Y416 in BMP9 and F411 in BMP10 (Fig 3a, red arrow), located in the top strand of finger 1 (Fig
225 3c, red arrows). This additional residue leads to a kink in this β-strand of BMP9 and BMP10,
226 resulting in a novel conformation that allows BMP9 and BMP10 to form unique interactions.
227 For example, this β-strand is in the core interaction site of BMP9 binding for ENG (Fig 5c),
228 making three backbone H-bonds with ENG to form an anti-parallel extended β-sheet [30]. In
229 addition, the side chain of the conserved Thr (413 in BMP9 and 408 in BMP10) also forms a H-
230 bond with that of ENG Q270, hence further contributing to the specificity of ENG for BMP9 and
231 BMP10 (Fig 5c).
232 Another polypeptide that binds to this conserved strand of BMP9 and BMP10 is the prodomain.
233 PDBePISA analysis of the pro-BMP9 structure (4YCG, mouse BMP9 prodomain bound to
234 human BMP9 GF-domain) [29] revealed that BMP9 and prodomain interactions are mostly
235 derived from three areas of the prodomain: the α2-helix, β1-strand and α5-helix (Fig 5d). The
236 prodomain β1-strand makes four mainchain H-bond interactions with the conserved region 2
237 in BMP9 to form an extended anti-parallel β-sheet (Fig 5e), which likely contributes to the
238 majority of the binding energy. Since the prodomains of BMP9 and BMP10 are highly
239 conserved, especially with respect to the contact residues in the α2-helix, β1-strand and α5-

helix (Fig 5d and Supplementary Fig 5), the structure of pro-BMP10 is very likely to resemble that of pro-BMP9.

Structure of pro-BMP9:ALK1 complex

It is interesting to note that in the BMP9 prodomain, residues from the α5-helix that bind to BMP9 are exclusively charged and only make side-chain interactions (Fig 5d). This helix interacts with BMP9 at the ALK1-binding site, and its density is missing in one of the two prodomain molecules in 4YCI [29], one of the two pro-BMP9 structures in the Protein Data Bank. This raises the question of whether ALK1 binding leads to displacement of the prodomain from BMP9. Indeed, a two-step mechanism for pro-BMP9 binding to the cell surface has been proposed [29], whereby ALK1 binding to pro-BMP9 causes the displacement of only the α5-helix and subsequent type II receptor binding leads to the complete prodomain displacement [29]. This theory would suggest the presence of a pro-BMP9:ALK1 complex in the initial stages of the signalling process. However, another report based on extensive SPR and ELISA analyses concluded that the binding of ALK1 alone displaced the entire prodomain [36]. To address this directly, we resolved the crystal structure of the human prodomain-bound BMP9 in complex with ALK1 (pro-BMP9:ALK1) to 3.3 Å. This is the first structure of a prodomain-bound ligand in complex with its high-affinity cognate receptor in the TGFβ superfamily.

The overall structure contains one copy of the BMP9 dimer, two copies of the ALK1 ECD and two copies of the prodomain. While the electron densities for BMP9 and ALK1 are excellent, the prodomains have overall poorer densities, with one copy heavily truncated and both copies missing the α5-helix (Fig 6a and Supplementary Fig 6&7). Regions of the prodomain that are in direct contact with BMP9, including the α2-helix and β1-strand, have good densities (Supplementary Fig 6b). The ALK1 and BMP9 components of this complex overlay very well with those in the BMP9:ALK1:ActRIIb complex structure (PDB:4FAO, with mainchain RMSD of

0.603 Å across BMP9:ALK1 mainchain atoms, Fig 6b), suggesting that the BMP9 GF-domain in the pro-BMP9 complex can bind to ALK1 as a rigid body with minimal conformational change. As for the prodomain, the regions in contact with the BMP9 GF-domain (α2-helix and β1-strand) overlay well with the prodomain in 4YCG (Fig 6c), whereas regions distal to the GF-domain are missing or overlay poorly. Overall the mainchain RMSD between the two prodomains in the pro-BMP9:ALK1 structure is 0.533 Å, and with the two prodomains in 4YCG, 0.666-0.678 Å (note that 4YCG contains mouse prodomain which may contribute to the slightly higher RMSD). Importantly, the mainchain extended β-sheet interactions from the conserved region 2 are maintained in the pro-BMP9:ALK1 structure (Fig 6d), suggesting that the contacts from the α5-helix may not be essential for the maintenance of BMP9:prodomain interactions.

Solution study of the pro-BMP9 and ALK1 interaction

To confirm that ALK1 ECD can form a ternary complex with full-length pro-BMP9, we performed an analytical gel filtration study using purified pro-BMP9 and ALK1 ECD (Fig 6e-h). We have recently shown that soluble endoglin (sENG) can displace the prodomain effectively from the pro-BMP9 complex, with the displaced prodomain readily detectable as a different peak by analytical gel filtration[37], so we included sENG with pro-BMP9 as a control. As shown in Figure 6e&f, pro-BMP9 and sENG alone eluted at peaks 1 and 6, respectively. When pro-BMP9 was mixed with 2-fold molar excess of ALK1, a pro-BMP9:ALK1 complex could be detected under peak 2, with excess ALK1 eluting under peak 3. The control experiment with a mixture of pro-BMP9 and sENG showed the sENG:BMP9 complex eluted under peak 4 and the dissociated prodomain eluted under a different peak (peak 5). Furthermore, western blots of the consecutive fractions with anti-BMP9 prodomain antibody confirmed that mixing of pro-BMP9 with ALK1 did not shift the peak of the prodomain, whereas mixing pro-BMP9 with sENG led to a shift of the prodomain peak to later fractions that are smaller than 66kDa protein

marker (Fig 6e&g). Similarly, we detected the pro-BMP10:ALK1 complex and excess ALK1 when mixing pro-BMP10 with ALK1 (Supplementary Fig 8a). Importantly, the prodomains in the pro-BMP9:ALK1 and pro-BMP10:ALK1 complexes are in the intact form, i.e. the α5-helix is still present, as confirmed by the size of the prodomain on the SDS-PAGE (Fig 6f and Supplementary Fig 8a). This study confirms that ALK1 can bind to the full-length pro-BMP9 and pro-BMP10 complex without displacing the entire prodomain (Fig 6h). A similar conclusion can also be drawn from the native gel analysis (Supplementary Fig 8b). Pro-BMP9 runs as three bands on the native PAGE: the GF-domain (band 1), the prodomain (band 3) and the pro-BMP9 complex (band 2). Upon mixing with ALK1 ECD (band 4), newly appeared bands containing the ALK1:BMP9 complex (band 5) as well as the pro-BMP9:ALK1 complex (band 7) could be readily detected.

CV2 does not inhibit BMP9 signalling

The conserved region 2 corresponds to the same region where CV2 binds to BMP2 (Fig 7a)[38]. A detailed analysis of the CV2:BMP2 structure (PDB:3BK3)[38] revealed that CV2 forms four backbone H-bond interactions with the same top strand of finger 1 in BMP2. Since BMP9 and BMP10 have an insertion and adopt a different conformation in this strand, we hypothesised that CV2 would not be able to interact with BMP9 as it does to BMP2, even though a previous publication using a reporter assay suggests that CV2 inhibits BMP9 signalling [11]. We first tested whether CV2 could inhibit BMP9 or pro-BMP9 signalling in the physiologically relevant cell type PAECs; no CV2 inhibition was observed even when CV2 was applied at a 250-fold molar excess using either a Smad1/5 phosphorylation assay (Fig 7b) or measuring *ID1* gene induction (Fig 7c). As a positive control, we detected CV2 inhibition of BMP4 signalling in pulmonary artery smooth muscle cells (PASMCs) at 10- or 20-fold molar excess using the same protocol (Fig 7d). To further confirm that CV2 is capable of inhibiting BMP2 but not BMP9

signalling, we performed parallel BMP2 and BMP9 signalling assays in a single cell type, C2C12 cells, by monitoring ALP induction. As shown in Figure 7e, both BMP2 and BMP9 induced robust ALP activity in C2C12 cells. While the presence of CV2 inhibited BMP2-induced ALP activity potently and in a dose-dependent manner, no inhibition was detected for BMP9-mediated ALP induction. These cell assays verified our structural analysis that CV2 does not inhibit BMP9 signalling.

Modifying BMP9 signalling specificity by mutagenesis

Our structural and sequence analyses suggest that protein-protein recognition between BMPs and their receptors is regulated by a tripartite mechanism, whereby one set of residues are conserved across all BMPs, a second set are conserved within each BMP subfamily and the remaining residues are unique for each BMP ligand. This would suggest that the interface residues that are not conserved between BMP9 and BMP10 likely contribute to the features that vary between the two ligands. It has been shown that BMP9 is very potent in inducing ALP activity in C2C12 cells *in vitro* and heterotopic bone formation *in vivo*, whereas BMP10 does not have such activities [39]. We therefore questioned whether it is possible to generate variants of BMP9 with less or no osteogenic activity by mutating non-conserved interface residues from BMP9 to BMP10 (those highlighted in yellow in Fig 4a). Indeed, 4 out of the 7 mutants showed reduced ALP-induction activity in C2C12 cells compared to wild type (WT) BMP9, in particular F362Y and D366E mutations results in complete loss of BMP9-induced ALP activity under the experimental conditions (Fig 8a). A similar pattern was also observed when monitoring the *Id1*-gene induction by BMP9 and its variants in C2C12 cells (Supplementary Fig 9). We further measured type I receptor binding affinities of BMP9, BMP10 and the BMP9 variant D366E which has lost ALP-induction activity in C2C12 cells. As shown in Supplementary Figure 10, pro-BMP9, pro-BMP9 D366E and pro-BMP10 all bind to ALK1-Fc with similar affinities. But for

binding to the ALK2-Fc, we can only detect the binding of pro-BMP9 and BMP9 GF-domain, not pro-BMP10 or pro-BMP9 D366E, confirming the D to E mutation at position 366 of BMP9 abolishes its ability to bind ALK2. Since BMP10 was shown to be non-osteogenic *in vivo* [39], we subjected pro-BMP9 D366E to an *in vivo* osteogenic assay, along with BMP2 GF-domain, pro-BMP9 and pro-BMP10 controls. To our surprise, in this *in vivo* assay with purified recombinant proteins, not only did pro-BMP9 D366E induce bone-formation, but pro-BMP10 itself was also an osteogenic BMP (Fig 8b&c).

Discussion:

The endothelial ALK1-mediated BMP signalling pathway has attracted much attention due to its therapeutic potential for the treatment of cardiovascular disease and solid tumour. Understanding the molecular details of this pathway will facilitate the translation of therapies by improving their efficacy and specificity whilst minimising unwanted side effects. In this study, we provide essential insight into several key molecular details of the ligands involved in this signalling pathway.

Firstly, although BMP9 and BMP10 circulate in their prodomain-bound forms, most published signalling and functional assays have utilised GF-domains due to the unavailability of pro-BMP9 and pro-BMP10 from commercial sources. We have expressed full-length human BMP9 and BMP10 in mammalian cells and purified the circulating forms of the ligands under native conditions. We demonstrate that they are functionally equivalent ligands on vascular endothelial cells *in vitro* and bind to ALK1 ECD with similar affinities. This provides a strong rationale that pro-BMP10 could be administered like pro-BMP9 in treating PAH [23]. However, it is worth noting that this study focused on BMP9 and BMP10 with respect to ALK1-mediated signalling in endothelial cells. At higher concentrations, both BMP9 and BMP10 can signal through non-ALK1-dependent pathways [40,41] and thus may have different signalling capacity and functional consequences.

Secondly, by solving the crystal structure of the BMP10:ALK1 complex and comparing it to published structures, we have identified three regions that are highly conserved between BMP9 and BMP10. The conserved region 1 accounts for ALK1 specificity. The conserved region 2 defines the specificity for ENG, prodomain and possibly the type II receptor as well. The conserved region 3 is located in the middle part of the BMP dimer. The crystal structure of pro-

myostatin suggests that C-terminal part of the prodomain could potentially interact with myostatin GF-domain residues in this region [42]. A crystal structure of unprocessed proBMP9 or proBMP10 will be required to address this question.

The type I and type II receptor binding sites have a common feature in that each possesses residues that are conserved among all BMPs (red surface in Fig 4a and Fig 5a), and residues that are variable and determine BMP subgroup specificity. This is reminiscent of a well-characterised protein-protein recognition between four colicin DNases and their cognate immunity proteins. This family of closely related and structurally homologous proteins achieve specificity by a dual recognition mechanism, whereby a conserved region contributes to the major binding energy whilst a variable region modifies the interaction by further contributing positively in cognate interactions or negatively in non-cognate interactions [43,44]. There are 15 BMP molecules in humans, which signal through four type I and three type II receptors. Therefore, more complicated mechanisms are required for the regulation of specific protein-protein interactions within the BMP system. We identified a tripartite mechanism here which could explain the specificity between BMP-receptor interactions. The 16 conserved residues in the conserved regions 1 to 3 identified in this study distinguish BMP9 and BMP10 from other members of the BMP family, in particular those within the type I site determine the ALK1-signalling specificity.

The structure of the pro-BMP9:ALK1 complex is the first of such a complex in the TGFβ superfamily. We observed significant proteolysis of the prodomain in this crystal structure (Supplementary Fig 7). Although it is possible that the excessive proteolysis was due to a crystallisation artefact, the digested regions do not make direct crystal contacts and thus there is no evidence to suggest that the proteolysis would favour crystal formation. We speculate

that the binding of ALK1 to pro-BMP9 may destabilise the prodomain, rendering it more susceptible to proteolysis; hence only the regions in direct contact with BMP9 are highly ordered due to interaction restraints. Nevertheless, this structure suggests that ALK1 ECD binding to pro-BMP9 does not lead to the dissociation of the prodomain, in contrast to a previous report [36]. We further validated this conclusion using analytical gel filtration with sENG as a control [37]. Our result is in agreement with Mi *et al* [29] that ALK1 binding only displace the α5-helix, not the entire prodomain from BMP9.

Structural analysis of the conserved region 2 revealed a distinct conformation adopted by BMP9 and BMP10 due to one amino acid insertion, prompted us to question whether CV2 could inhibit BMP9 and BMP10 signalling as reported previously [11,12]. Using a range of cell-based signalling assays, we have conclusively shown that CV2 does not inhibit BMP9 signalling. This observation has important translational implications; for instance, if BMP9 is to be developed into a therapy for PAH, the presence of any circulating ligand traps must be taken into account.

Finally, during the validation of the structural findings, we performed mutagenesis of BMP9 to modify its specificity and evaluated its osteogenic activity *in vitro* and *in vivo*. We found unexpectedly that BMP10 is also an osteogenic BMP that can promote heterotopic bone-formation *in vivo*, in contrast to a previous report [39]. This is likely due to limitations in the methodology employed in the previous study, whereby C2C12 cells infected with adenoviral constructs containing the BMP10 gene were used for the ALP activity and *in vivo* bone-forming assay. It is not known in that study whether the BMP10 produced from transfected C2C12 cells was fully processed and active. In our study, we used purified, fully processed recombinant pro-BMP10 with activity validated in PAECs [5]. Importantly, our data also demonstrate that lack

of ALP activity *in vitro* does not necessarily predict lack of osteogenic activity *in vivo*. More studies are required to understand molecular mechanisms that determine the bone-inducing activity of BMP9 and BMP10.

In summary, using a combination of signalling assays, protein biochemistry and X-ray crystallography, we provide extensive and detailed molecular insights into ALK1-mediated signalling by circulating forms of BMP9 and BMP10. Such knowledge will provide essential information for improving the specificity and efficacy of therapies that target the endothelial BMP signalling pathways.

Methods:

Materials. Rabbit antibody against phospho-Smad1/5 (pSmad1/5, cat. No. 9516) was purchased from Cell Signalling Technology. Mouse monoclonal anti-α-tubulin (cat. No. T6199) was purchased from Sigma-Aldrich. Secondary anti-rabbit horseradish peroxidase (HRP) antibody (cat. No. P0448) and anti-mouse HRP antibody (cat. No. P0447) were both from Dako. Plasmid purification kits and RNA extraction kits were purchased from Qiagen. DMEM and CDCHO media were purchased from Thermo Fisher Scientific. Pulmonary artery endothelial cells (PAECs, cat. No. CC-2530) and endothelial growth medium (EGM2) were purchased from Lonza. HEK EBNA cells (cat. No. CRL-10852) and C2C12 cells (cat. No. CRL-1772) were purchased from ATCC. Chromatography columns were purchased from GE Healthcare. All crystallisation reagents were purchased from Hampton Research Inc and Molecular Dimensions. Human GF-domains of BMP2, BMP9 and BMP10, CV2, ALK1-Fc and ALK2-Fc were all purchased from R&D Systems.

Expression and purification of the ALK1 ECD. Human ALK1 cDNA (NM_000020) encoding amino acids 22-118 was cloned into pET39b (70090, Novagen) between NcoI and NotI sites to create a fusion protein DsbA-$(His)_6$-ALK1 ECD. A TEV (Tobacco Etch Virus nuclear inclusion A endopeptidase) protease cleavage site was introduced at the N-terminus of the ALK1 ECD to facilitate release of the untagged ECD. The construct was confirmed by DNA sequencing and transformed into bacterial strain Rosetta DE3 (70954, Novagen) for protein expression. Cells were grown to mid-log phase followed by isopropyl β-D-thiogalactopyranoside induction and further incubation at 22°C overnight. ALK1 ECD was purified from periplasmic fractions following the method described previously for the BMPRII ECD [5]. Briefly, total periplasmic proteins were extracted following the pET System Manual (Novagen) and His-tagged fusion proteins were purified on a 5ml nickel-nitrilotriacetic acid column (GE Healthcare). Fractions

containing the fusion protein were pooled, dialysed into Tris Buffered Saline, and incubated overnight with His-tagged TEV protease. The mixture was passed through a pre-charged nickel-nitrilotriacetic acid column to remove His-tagged DsbA and TEV protease. ALK1 ECD, which was in the flow-through and wash solution, was concentrated and further purified by gel filtration on a Superdex 75 column.

Expression and purification of pro-BMP9 and pro-BMP10. Full-length human BMP9 cDNA was cloned into pCEP4 (V04450, Invitrogen) between HindIII and XhoI sites and verified by DNA sequencing. Cloning of full length human pro-BMP10, transfection and purification of pro-BMP9 and pro-BMP10 were achieved following previously described protocols [5]. Briefly, pCEP4 constructs containing either proBMP9 or proBMP10 were purified using Qiagen midi prep kit. HEK EBNA cells were seeded in 10 triple flasks and grown to 50-80% confluency before being transfected using polyethylenimine. Serum-free CDCHO medium was applied from Day 2 and conditioned media were harvested every 3-4 days over two weeks. To facilitate the processing, human full-length furin cDNA, also cloned in pCEP4, was co-transfected with proBMP10.

To purify pro-BMP9 or pro-BMP10, 5 litres of conditioned medium was loaded onto two tandemly linked 5ml Hitrap Q columns, pre-equilibrated in 20mM Tris.HCl, pH7.4. After elution with NaCl gradient, fractions containing pro-BMP9 or pro-BMP10 were identified on a non-reducing SDS-PAGE, pooled, concentrated using VivaSpin columns (Sartorius) and loaded onto a HiLoad 16/600 Superdex 200 pg gel filtration column pre-equilibrated in 20 mM Tris.HCl, 50 mM NaCl. Fractions containing target proteins were identified by SDS-PAGE and Coomassie staining, further purified on a MonoP 5/200 GL column which was pre-equilibrated in 20 mM Tris.Cl, pH7.4. After elution with NaCl gradient, target proteins were pooled and subject to a

final purification step on a Superdex 200 column, pre-equilibrated in 20 mM Tris.HCl, pH7.4, 150 mM NaCl.

Expression and purification of sENG. The expression and purification of sENG have been described recently [37]. Briefly, residue 1-586 of human ENG cDNA was cloned into pCEP4 with a C-terminal 6xHis tag and sequence was confirmed by DNA sequencing. Plasmids containing sENG were transiently transfected into HEK EBNA cells in DMEM containing 5% FBS before changing into CDCHO expression media. Conditioned medium was harvested every 3-4 days for up to 2 weeks and used for purification. To purify sENG, 5 litres of conditioned medium were loaded onto a 5 ml HiTrap Excel column (GE Healthcare) pre-equilibrated in Buffer A (50 mM TrisHCl, pH7.4, 500 mM NaCl, 5 mM imidazole). After wash, sENG was eluted with 5-1000 mM imidazole gradient in buffer A. Fractions containing sENG were identified on SDS-PAGE, pooled and dialysed against 50mM Tris.HCl, pH7.4, 50 mM NaCl and then loaded onto a 5 ml HiTrap Q HP column. After eluting with a NaCl gradient, fractions containing sENG were identified by non-reducing SDS-PAGE, pooled and further purified on a Superdex 200 16/600 gel filtration column.

Endothelial cell signalling assays. Human PAECs were grown in EGM2 with 10% FBS until 90% confluent before undergoing quiescence for 16 hours in EGM2 with 0.1% FBS. Cells were treated with GF-domains of BMP9 and BMP10, or pro-BMP9 and pro-BMP10 with detailed conditions described in legends to Figure 1, 7&8. Immunoblotting and qPCR analyses were carried out as detailed below.

Immunoblotting for detecting Smad1/5 phosphorylation. Cell lysates were quantified using Detergent Compatible (DC) ™ Protein Assay Kit II (cat. No. 5000112; Bio-Rad) following

which 40 μg of protein was loaded and fractionated on a 10% SDS-PAGE. After transfer and blocking, the membranes were incubated with anti-pSmad1/5 antibody (1:300 dilution) followed by wash and secondary anti-rabbit HRP antibody (1:2000 dilution). After further wash and detection with chemiluminescence reagents (GE Biosceince), the blots were washed in PBS and re-probed with mouse anti-α-tubulin antibody (1:2000 dilution). After washing and incubating with secondary anti-mouse HRP antibody (1:2000 dilution), the target protein was revealed using chemiluminescence kit.

RNA extraction and qPCR analysis. At the end of the treatment, cells were washed and snap-frozen. Total RNA was extracted using RNeasy Plus Mini kit and reverse transcription was carried out using High-Capacity cDNA Reverse Transcription Kit (Applied Biosystems) following manufacturer's instruction. The following primers were used for the qPCR analysis: human *ID1*: 5'-CTGCTCTACGACATGAACGGC, 5'-TGACGTGCTGGAGAATCTCCA; human β-2-microglobulin (*B2M*): 5'-CTCGCGCTACTCTCTCTTTCT, 5'-CATTCTCTGCTGGATGACGTG; The reactions were carried out on a StepOnePlus™ cycler (Applied BioSystems) and the relative expression of *ID1* was normalised to *B2M* using the ΔΔCT method, shown as fold-change relative to control samples.

Microarray analysis. Four human PAEC lines were grown as described above and treated with pro-BMP9 or pro-BMP10 (both at 0.3 ng ml^{-1} GF-domain final concentration) for 1.5 hours before cells were harvested for mRNA extraction. Microarray experiments were performed at Cambridge Genomic Services, using a human Gene 2.1 ST Array Plate (Affymetrix, Wooburn Green, UK) in combination with WT PLUS amplification kit (Affymetrix) according to the manufacturer's instructions. Following data processing using package Oligo (version 1.40.2) in

R (version 3.3) [45], normalisation was carried out using Robust Multichip Analysis (RMA)[46], and comparisons were performed using the limma package (version 3.32.1) [47]. The results were corrected for multiple testing using False Discovery Rate (FDR).

Surface Plasmon Resonance Analysis. Receptor-ligand binding experiments were performed using the Biacore T100 biosensor (Biacore/GE Healthcare). ALK1-Fc or ALK1 monomer was immobilised onto a Series S research grade CM5 sensor chip by amine-coupling at a density of 800 or 270 resonance units respectively. Flow cell 1 was used as the blank reference cell for subtraction during analysis. For kinetic measurements, a concentrated series of BMP9 GF-domain, pro-BMP9, BMP10 GF-domain or pro-BMP10 were injected in duplicate over the flow cells at a flow rate of 30 µl min^{-1} in a buffer containing 0.01 M HEPES, pH7.4, 0.5 M NaCl, 3 mM EDTA, 0.5 mg ml^{-1} BSA and 0.01% (v/v) Surfactant P20 at 25 °C. The binding surface was regenerated with 4 M Guanidine Hydrochloride between each cycle by four short injections (8 sec each) at a flow rate of 30 µl min^{-1}. The kinetic rate constants were obtained by fitting the corrected data to a 1:1 interaction model using Biacore T100 Evaluation Software (version 2.0.3, GE Healthcare). The equilibrium binding constant K_D was determined by the ratio of binding rate constants k_d/k_a.

Structure of the BMP10:ALK1 complex. To purify the BMP10 GF-domain, pro-BMP10 was denatured in 7 M urea solution overnight before being loaded onto a 5 ml HiTrap S column equilibrated in a buffer containing 25 mM NaCl, 6 M urea and 20 mM Tris pH 7.4. Bound proteins were eluted with a 25 - 1000 mM NaCl gradient in 6 M urea, 20 mM Tris pH 7.4. Fractions containing BMP10 GF-domain disulphide-linked dimer were concentrated to 1 ml, then rapidly diluted with 19 ml of cold refolding buffer (1 M NaCl, 10% glycerol, 3% CHAPS, 2.5% glycine, 5 mM glutamic acid, pH4.0), and left to refold on a roller at 4°C for 10 days. The

refolded mixture was subject to centrifugation and the supernatant containing soluble, refolded BMP10 was recovered. Excess of purified ALK1 ECD was added directly to BMP10 in the refolding buffer, further incubated at 4°C overnight. The mixture was then concentrated to 1 ml and applied to a Superdex 200 16/600 column pre-equilibrated in 20 mM Tris pH 7.4 and 200 mM NaCl. Fractions containing BMP10:ALK1 ECD were identified by SDS-PAGE and Coomassie staining, pooled and concentrated to 1.2 mg ml^{-1} for crystallisation. Hanging-drop crystallisation trials, using 1 µl protein and 1 µl reservoir solution, were set up and diffraction quality crystals were obtained over 1 month in 17% PEG 3350, 0.175 M NH_4I, 0.1 M HEPES pH 7.8 at 22°C. Crystals were cryo-protected in 30% glycerol, 19% PEG3350, 0.175 M NH_4I, 0.1 M HEPES pH 7.8 and flash-frozen in liquid nitrogen. Data were collected at 100 K at Diamond Light Source (DLS) on Beamline I03 at a wavelength of 0.9763 Å from a single crystal, and processed in space group $P6_522$ to 2.8 Å using iMOSFLM [48], Aimless [49] and Scala [50] in CCP4 suite (version 7.0-macosx-x86_64) [51]. The structure was solved by molecular replacement using Phaser [52], with BMP9 and ALK1 in 4FAO as the search models. Model building was carried out using Coot [53], and refined using REFMAC5 [54] and phenix.refine (version 1.11.1_2575) [55]. Validation was performed using MolProbity [56]. A second crystal form was subsequently obtained from Morpheus 2 screen condition 48 diluted with 30% water, which includes 0.07 M Amino acids (0.014 M DL-Glutamic acids monohydrate; 0.014 M DL-Alanine; 0.014 M Glycine; 0.014 M DL-Lysine monohydrochloride; 0.014 M DL-Serine), 0.07 M Buffer System 3 (0.07 M Tris(base)/BICINE) pH 8.5, 35% Precipitant Mix 4 (9% v/v MPD, 9% w/v PEG1000, 9% w/ PEG3350). Data collection was carried out at I03 (DLS) from a single crystal. Data was processed by DIALS [57] and aimless in space group $P6_522$ to 2.3 Å. The structure was solved by molecular replacement using Phaser, with the 2.8 Å BMP10:ALK1 ECD structure as the search model. Model building, refinement and validation were carried out as above. The dihedral angles of 96.59% and 97.16% of all amino-acid residues for the 2.3 Å and 2.8 Å

structures are in the favoured region and none in the disallowed region. All the data collection, data reduction, structure determination and refinement statistics are shown in Supplementary Table 1. The coordinates were deposited in the PDB with the access codes of 6SF1 (2.8 Å) and 6SF3 (2.3 Å). The two structures are almost identical, with small changes in some loop area (Supplementary Fig 2). The 2.3 Å resolution structure was used in the structural analysis in the results section.

Structure of the pro-BMP9:ALK1 complex. Purified pro-BMP9 was mixed with ALK1 ECD in a 1:1.5 molar ratio and incubated for 30 minutes at room temperature, following which the mixture was loaded onto a Superdex 200 16/600 column pre-equilibrated in 150 mM NaCl, 20 mM Tris pH 7.4. Fractions containing the pro-BMP9:ALK1 ECD complex were identified by SDS-PAGE and Coomassie staining, combined and concentrated to 10 mg ml^{-1} to set up crystallisation trials in hanging-drops, using 1 µl protein and 1 µl reservoir solution. Diffraction quality crystals were obtained by micro-seedings in 0.14 M K/Na tartrate, 14% PEG 3350 over 4 weeks at 22 °C. Data were collected at 100 K from a single crystal, cryo-protected in 25% glycerol in 0.14 M K/Na tartrate, 16% PEG 3350, at DLS on I04-1 at a wavelength of 0.9282 Å, processed in $P6_1$ to 3.3 Å. The structure was solved by molecular replacement using the BMP9:ALK1 structure from 4FAO and mouse prodomain from 4YCG as search models. Data processing, molecular replacement, model building and refinement were carried out using the software packages as described above. The dihedral angles of 95.72% of all amino-acid residues are in the favoured region and none in the disallowed region. The coordinates were deposited in the PDB with the access code 6SF2. All the data collection, data reduction, structure determination and refinement statistics are shown in Supplementary Table 1.

Structural analysis and sequence alignment. Structural analyses were performed and figures generated using PyMOL (The PyMOL Molecular Graphics System, Version 1.2r3pre, Schrödinger, LLC). For BMP10:ALK1 structure, the 2.3 Å structure was used for generating the final figures. Sequence alignments were performed using Clustal Omega[58]. Protein-protein interaction interfaces were analysed using the PDBePISA server (https://www.ebi.ac.uk/pdbe/pisa/)[33]. The numberings for all proteins in the alignments and structures begin at the start of the open reading frame i.e. Met1 of the signal peptide.

Analytical gel filtration. Purified pro-BMP9, sENG or pro-BMP10 (all at 100 µg) was mixed with a 2-fold molar excess of purified ALK1 ECD (in 150 mM NaCl, 20 mM Tris pH 7.4) or buffer control to a final volume of 200 µl. Above mixtures, alongside ALK1 ECD control, were run on a Superdex 200 10/300 size-exclusion column and 250 µl fractions were collected. Peak fractions from each run were assessed by SDS-PAGE, Coomassie or silver-staining. Traces were exported from AKTA Unicorn 6 control software, then aligned and displayed using Prism 6 software.

PASMC isolation. PASMCs were obtained from the lung resection specimens from the Papworth Hospital Research Tissue Bank. Ethical approval was obtained from the NRES Committee East of England -Cambridge East (reference number: 18/EE/0269). Informed consents were obtained from all donors. Isolation of PASMCs has been described previously [59]. Briefly, lung sections containing small vessels (< 2 mm diameter) were obtained. The lung parenchyma is dissected away and small vessels were cut into small pieces around 0.2 cm x 0.2 cm. The chopped vessel pieces were transferred to a T25 flask in DMEM medium supplemented with 20% fetal calf serum. Allowing approximately two weeks for cells to attach and expand before passage. PASMC cell type was confirmed by the characteristic elongated

morphology and immunostaining with calponin antibody. A negative mycoplasma test was obtained before the cells were used for the signalling assays. The PASMCs isolated from three individuals were used in the signalling assays.

Signalling assays in PASMCs. PASMCs were cultured in DMEM media with 10% FBS and antibiotics until 90% confluent before undergoing quiescence in DMEM with 0.1% FBS for 48 hours. Cells were treated with BMP4 GF-domain (25 ng ml^{-1}) in the presence or absence of CV2 at indicated concentrations for 15 minutes followed by protein extraction and pSmad1/5 immunoblotting as described above.

C2C12 cell signalling assays. C2C12 mouse myoblast cells were cultured in DMEM media supplemented with 10% FBS and antibiotics until about 70% confluent. Treatment mixture containing BMP2 or BMP9 with or without CV2 at indicated concentrations were made up to 1 ml with DMEM containing 0.25% FBS and antibiotics, followed by 30 minutes incubation at room temperature. The cells were washed twice with 1 ml DMEM containing 0.25% FBS before treatment mixture applied. After 68 hours, cells were snap-frozen using a dry ice ethanol bath and lysed with cold lysis buffer (1% Triton X-100 in PBS) and two freeze-thaw cycles. The cell lysates were collected and centrifuged at 17,000 g for 5 minutes at 4 °C to remove insoluble material. Protein quantification was performed on the cell lysates using the DC™ Protein Assay Kit II (BioRad). ALP activity was measured using a 96-well plate. Duplicate wells were prepared with 20 µg of cell lysate protein in a total of 50 µl lysis buffer before 100 µl of pNPP substrate was added (Sigma-Aldrich) in 0.1 M glycine buffer, pH 10.4, containing 1 mM $MgCl_2$ and 1 mM $ZnCl_2$. The plate was covered in foil and incubated at 37 °C for 30 minutes, following which the absorbance was periodically read at 405 nm on a Microplate Reader.

BMP9 mutagenesis and *in vitro* signalling assays. A panel of BMP9 mutants was generated by replacing specified residues at the type I receptor site with equivalent residues from BMP10 using site-directed mutagenesis. Mutations were verified by DNA sequencing. Mutant proteins, alongside WT pro-BMP9, were expressed in HEK-EBNA cells in T25 flasks. Because mutations in the BMP9 GF-domain may change the antibody binding epitope, current published ELISA methods which use antibodies against the GF-domain are not suitable for quantifying the mutant proteins in the transfected medium. On the other hand, prodomain and the GF-domain are produced from the same polypeptide chain and processed in a 1:1 ratio, hence the ratio of prodomain of BMP9 mutant to WT in the conditioned media will be identical to the ratio of mature GF-domains. We therefore quantified Pro-BMP9 WT and mutant proteins in the conditioned media from each transfection following a previously published method as below [28]. The conditioned media were subject to two repeats of anti-prodomain western blots and the ratio of band intensity of mutants to WT calculated. The concentration of WT BMP9 in the transfection medium was determined by ELISA using BMP9 from R&D Systems as standards. The concentrations of the mutant proteins were calculated using the ratio obtained from anti-prodomain blots. Endothelial cell and C2C12 cell signalling assays were carried our as detailed above. Fold changes relative to the WT were quantified from three independent HEK-EBNA transfection and quantification experiments. Means ± SEM are shown.

***In vivo* heterotopic ossification (HO) assay.**

All in vivo animal studies were performed in accordance with the UK Home Office regulations (Project Licence: PPL PAE2D0A13) and ethical approval was obtained from the University of Cambridge's Animal Welfare and Ethical Review Board.

Male C57/BL6 mice (Charles Rivers UK Ltd) of 7-8 weeks' old were housed in groups of 4 in individually vented cages with free access to food and water. After an acclimatization period of

10 days, they were anaesthetised with isoflurane in O_2 before the implantation of reduced growth factor Matrigels (Corning, Growth Factor Reduced, cat. No. 356231) loaded with purified pro-BMP9, pro-BMP9 D366E, pro-BMP10 or BMP2 GF-domain (from R&D Systems) into the mid belly of the Quadriceps Femoris (QF) muscle. Because BMP9-induced heterotopic bone formation requires local muscle damage which could be achieved by cardiotoxin injection, we performed the bone formation assay in the presence and absence of cardiotoxin [60]. Cardiotoxin (40 µl 10 µM from Naja Pallida, Latoxan, Portes les Valence, France. cat. No. L8102) was injected two days prior to the Matrigel/BMP implant in to the QF of one leg to induce local inflammation. *Ex vivo* morphological analysis of heterotopic bone formation was carried out 14 days after the BMP application by microCT (Bruker, SkyScan 1172). 3D MicroCT images (Fig 8c) were reconstructed from 180 radiograph projections using filtered back projection in CTvox software (Bruker). The HO volume was calculated from contiguous 5 µm thick coronal CT slices. The HO area per slice was measured by importing the CT sections into ImageJ and the HO segmented from the surrounding muscle and bone by lower and upper threshold techniques. The HO volume was calculated from the measured area and the interslice thickness. Sections of the tissues containing the heterotopic bone were examined by Hematoxylin & eosin staining and Masson's trichrome staining.

Data Availability. Coordinates and structure factors for all structures have been deposited to the Protein Data Bank, with the accession numbers of 6SF1, 6SF2 and 6SF3. Microarray data have been deposited to Gene Expression Omnibus, with the accession number of GSE134890. All additional experimental data are available from the corresponding author on request. The source data underlying Figs 1**a**, 7**b-e**, 8**a**&**b** and Supplementary Fig 9 are provided as a Source Data file.

References:

1 Seki, T., Yun, J. & Oh, S. P. Arterial endothelium-specific activin receptor-like kinase 1 expression suggests its role in arterialization and vascular remodeling. *Circ. Res.* **93**, 682-689, (2003).

2 David, L., Mallet, C., Mazerbourg, S., Feige, J. J. & Bailly, S. Identification of BMP9 and BMP10 as functional activators of the orphan activin receptor-like kinase 1 (ALK1) in endothelial cells. *Blood* **109**, 1953-1961, (2007).

3 Walsh, D. W., Godson, C., Brazil, D. P. & Martin, F. Extracellular BMP-antagonist regulation in development and disease: tied up in knots. *Trends Cell Biol.* **20**, 244-256, (2010).

4 Bidart, M. *et al.* BMP9 is produced by hepatocytes and circulates mainly in an active mature form complexed to its prodomain. *Cell. Mol. Life Sci.* **69**, 313-324, (2012).

5 Jiang, H. *et al.* The Prodomain-bound Form of Bone Morphogenetic Protein 10 Is Biologically Active on Endothelial Cells. *J. Biol. Chem.* **291**, 2954-2966, (2016).

6 Shi, M. *et al.* Latent TGF-beta structure and activation. *Nature* **474**, 343-349, (2011).

7 Ricard, N. *et al.* BMP9 and BMP10 are critical for postnatal retinal vascular remodeling. *Blood* **119**, 6162-6171, (2012).

8 Chen, H. *et al.* Context-dependent signaling defines roles of BMP9 and BMP10 in embryonic and postnatal development. *Proc. Natl. Acad. Sci. U. S. A.* **110**, 11887-11892, (2013).

9 Townson, S. A. *et al.* Specificity and structure of a high affinity activin receptor-like kinase 1 (ALK1) signaling complex. *J. Biol. Chem.* **287**, 27313-27325, (2012).

10 Castonguay, R. *et al.* Soluble endoglin specifically binds bone morphogenetic proteins 9 and 10 via its orphan domain, inhibits blood vessel formation, and suppresses tumor growth. *J. Biol. Chem.* **286**, 30034-30046, (2011).

11 Yao, Y. *et al.* Crossveinless 2 regulates bone morphogenetic protein 9 in human and mouse vascular endothelium. *Blood* **119**, 5037-5047, (2012).

12 Jumabay, M. *et al.* Combined effects of bone morphogenetic protein 10 and crossveinless-2 on cardiomyocyte differentiation in mouse adipocyte-derived stem cells. *J. Cell. Physiol.* **233**, 1812-1822, (2018).

13 Garcia de Vinuesa, A., Abdelilah-Seyfried, S., Knaus, P., Zwijsen, A. & Bailly, S. BMP signaling in vascular biology and dysfunction. *Cytokine Growth Factor Rev.* **27**, 65-79, (2016).

14 David, L. *et al.* Bone morphogenetic protein-9 is a circulating vascular quiescence factor. *Circ. Res.* **102**, 914-922, (2008).

15 McAllister, K. A. *et al.* Endoglin, a TGF-beta binding protein of endothelial cells, is the gene for hereditary haemorrhagic telangiectasia type 1. *Nat. Genet.* **8**, 345-351, (1994).

16 Johnson, D. W. *et al.* Mutations in the activin receptor-like kinase 1 gene in hereditary haemorrhagic telangiectasia type 2. *Nat. Genet.* **13**, 189-195, (1996).

17 Wooderchak-Donahue, W. L. *et al.* BMP9 mutations cause a vascular-anomaly syndrome with phenotypic overlap with hereditary hemorrhagic telangiectasia. *Am. J. Hum. Genet.* **93**, 530-537, (2013).

18 International, P. P. H. C. *et al.* Heterozygous germline mutations in BMPR2, encoding a TGF-beta receptor, cause familial primary pulmonary hypertension. *Nat. Genet.* **26**, 81-84, (2000).

19 Wang, G. *et al.* Novel homozygous BMP9 nonsense mutation causes pulmonary arterial hypertension: a case report. *BMC Pulm. Med.* **16**, 17, (2016).

20 Trembath, R. C. *et al.* Clinical and molecular genetic features of pulmonary hypertension in patients with hereditary hemorrhagic telangiectasia. *N. Engl. J. Med.* **345**, 325-334, (2001).

21 Harrison, R. E. *et al.* Transforming growth factor-beta receptor mutations and pulmonary arterial hypertension in childhood. *Circulation* **111**, 435-441, (2005).

22 Ormiston, M. L., Upton, P. D., Li, W. & Morrell, N. W. The promise of recombinant BMP ligands and other approaches targeting BMPR-II in the treatment of pulmonary arterial hypertension. *Glob Cardiol Sci Pract* **2015**, 47, (2015).

23 Long, L. *et al.* Selective enhancement of endothelial BMPR-II with BMP9 reverses pulmonary arterial hypertension. *Nat. Med.* **21**, 777-785, (2015).

24 Duffy, A. G. *et al.* Phase I and Preliminary Phase II Study of TRC105 in Combination with Sorafenib in Hepatocellular Carcinoma. *Clin. Cancer Res.* **23**, 4633-4641, (2017).

25 Jimeno, A. *et al.* A phase 2 study of dalantercept, an activin receptor-like kinase-1 ligand trap, in patients with recurrent or metastatic squamous cell carcinoma of the head and neck. *Cancer* **122**, 3641-3649, (2016).

26 Apolo, A. B. *et al.* A Phase II Clinical Trial of TRC105 (Anti-Endoglin Antibody) in Adults With Advanced/Metastatic Urothelial Carcinoma. *Clin. Genitourin. Cancer* **15**, 77-85, (2017).

27 Brown, M. A. *et al.* Crystal structure of BMP-9 and functional interactions with pro-region and receptors. *J. Biol. Chem.* **280**, 25111-25118, (2005).

28 Wei, Z., Salmon, R. M., Upton, P. D., Morrell, N. W. & Li, W. Regulation of Bone Morphogenetic Protein 9 (BMP9) by Redox-dependent Proteolysis. *J. Biol. Chem.* **289**, 31150-31159, (2014).

29 Mi, L. Z. *et al.* Structure of bone morphogenetic protein 9 procomplex. *Proc. Natl. Acad. Sci. U. S. A.* **112**, 3710-3715, (2015).

30 Saito, T. *et al.* Structural Basis of the Human Endoglin-BMP9 Interaction: Insights into BMP Signaling and HHT1. *Cell Rep* **19**, 1917-1928, (2017).

31 Allendorph, G. P., Vale, W. W. & Choe, S. Structure of the ternary signaling complex of a TGF-beta superfamily member. *Proc. Natl. Acad. Sci. U. S. A.* **103**, 7643-7648, (2006).

32 Kotzsch, A., Nickel, J., Seher, A., Sebald, W. & Muller, T. D. Crystal structure analysis reveals a spring-loaded latch as molecular mechanism for GDF-5-type I receptor specificity. *EMBO J.* **28**, 937-947, (2009).

33 Krissinel, E. & Henrick, K. Inference of macromolecular assemblies from crystalline state. *J. Mol. Biol.* **372**, 774-797, (2007).

34 Greenwald, J. *et al.* The BMP7/ActRII extracellular domain complex provides new insights into the cooperative nature of receptor assembly. *Mol. Cell* **11**, 605-617, (2003).

35 Weber, D. *et al.* A silent H-bond can be mutationally activated for high-affinity interaction of BMP-2 and activin type IIB receptor. *BMC Struct. Biol.* **7**, 6, (2007).

36 Kienast, Y. *et al.* Rapid Activation of Bone Morphogenic Protein 9 by Receptor-mediated Displacement of Pro-domains. *J. Biol. Chem.* **291**, 3395-3410, (2016).

37 Lawera, A. *et al.* Role of soluble endoglin in BMP9 signaling. *Proc. Natl. Acad. Sci. U. S. A.*, (2019).

38 Zhang, J. L. *et al.* Crystal structure analysis reveals how the Chordin family member crossveinless 2 blocks BMP-2 receptor binding. *Dev. Cell* **14**, 739-750, (2008).

39 Kang, Q. *et al.* Characterization of the distinct orthotopic bone-forming activity of 14 BMPs using recombinant adenovirus-mediated gene delivery. *Gene Ther.* **11**, 1312-1320, (2004).

40 Luo, J. *et al.* TGFbeta/BMP type I receptors ALK1 and ALK2 are essential for BMP9-induced osteogenic signaling in mesenchymal stem cells. *J. Biol. Chem.* **285**, 29588-29598, (2010).

41 Mazerbourg, S. *et al.* Identification of receptors and signaling pathways for orphan bone morphogenetic protein/growth differentiation factor ligands based on genomic analyses. *J. Biol. Chem.* **280**, 32122-32132, (2005).

42 Cotton, T. R. *et al.* Structure of the human myostatin precursor and determinants of growth factor latency. *EMBO J.* **37**, 367-383, (2018).

43 Li, W. *et al.* Dual recognition and the role of specificity-determining residues in colicin E9 DNase-immunity protein interactions. *Biochemistry* **37**, 11771-11779, (1998).

44 Li, W. *et al.* Highly discriminating protein-protein interaction specificities in the context of a conserved binding energy hotspot. *J. Mol. Biol.* **337**, 743-759, (2004).

45 Carvalho, B. S. & Irizarry, R. A. A framework for oligonucleotide microarray preprocessing. *Bioinformatics* **26**, 2363-2367, (2010).

46 Irizarry, R. A. *et al.* Exploration, normalization, and summaries of high density oligonucleotide array probe level data. *Biostatistics* **4**, 249-264, (2003).

47 Ritchie, M. E. *et al.* limma powers differential expression analyses for RNA-sequencing and microarray studies. *Nucleic Acids Res.* **43**, e47, (2015).

48 Battye, T. G., Kontogiannis, L., Johnson, O., Powell, H. R. & Leslie, A. G. iMOSFLM: a new graphical interface for diffraction-image processing with MOSFLM. *Acta Crystallogr. D Biol. Crystallogr.* **67**, 271-281, (2011).

49 Evans, P. R. & Murshudov, G. N. How good are my data and what is the resolution? *Acta Crystallogr. D Biol. Crystallogr.* **69**, 1204-1214, (2013).

50 Evans, P. Scaling and assessment of data quality. *Acta Crystallogr. D Biol. Crystallogr.* **62**, 72-82, (2006).

51 Winn, M. D. *et al.* Overview of the CCP4 suite and current developments. *Acta Crystallogr. D Biol. Crystallogr.* **67**, 235-242, (2011).

52 McCoy, A. J. *et al.* Phaser crystallographic software. *Journal of applied crystallography* **40**, 658-674, (2007).

53 Emsley, P., Lohkamp, B., Scott, W. G. & Cowtan, K. Features and development of Coot. *Acta Crystallogr. D Biol. Crystallogr.* **66**, 486-501, (2010).

54 Murshudov, G. N. *et al.* REFMAC5 for the refinement of macromolecular crystal structures. *Acta Crystallogr. D Biol. Crystallogr.* **67**, 355-367, (2011).

55 Afonine, P. V. *et al.* Towards automated crystallographic structure refinement with phenix.refine. *Acta Crystallogr. D Biol. Crystallogr.* **68**, 352-367, (2012).

56 Chen, V. B. *et al.* MolProbity: all-atom structure validation for macromolecular crystallography. *Acta Crystallogr. D Biol. Crystallogr.* **66**, 12-21, (2010).

57 Winter, G. *et al.* DIALS: implementation and evaluation of a new integration package. *Acta Crystallogr D Struct Biol* **74**, 85-97, (2018).

58 Sievers, F. *et al.* Fast, scalable generation of high-quality protein multiple sequence alignments using Clustal Omega. *Mol. Syst. Biol.* **7**, 539, (2011).

59 Yang, X. *et al.* Dysfunctional Smad signaling contributes to abnormal smooth muscle cell proliferation in familial pulmonary arterial hypertension. *Circ. Res.* **96**, 1053-1063, (2005).

60 Leblanc, E. *et al.* BMP-9-induced muscle heterotopic ossification requires changes to the skeletal muscle microenvironment. *J. Bone Miner. Res.* **26**, 1166-1177, (2011).

61 Groppe, J. *et al.* Structural basis of BMP signalling inhibition by the cystine knot protein Noggin. *Nature* **420**, 636-642, (2002).

Acknowledgement:

This work was supported by the British Heart Foundation grants PG/12/54/29734, PG/15/39/31519 and PG/17/1/32532 to W.L. and N.W.M. We would like to thank Prof. Peter ten Dijke for constructive comments, Diamond Light Source for beamtime (proposals MX11235 and MX15916), and the support by the staff on beamlines I03 and I04-1 for assistance with crystal testing and data collection. We also thank the support from Cambridge Genomic Service, in particular Dr Emily Clemente and Dr Julien Bauer, during the microarray data analysis.

Author contributions: R.M.S., J.G., J.H.W., Z.T., J.S.B., A.L. and M.Y. collected and analysed the data. R.M.S., D.J.G, J.R., N.W.M. and W.L. designed the experiments and analysed the data. W.L. performed structural and sequence analyses, coordinated the study and drafted the manuscript. All authors contributed to the writing of the paper.

Competing interests: N.W.M. and W.L. are co-founders of Morphogen-IX. D.J.G. and J.R. are co-founders of RxCelerate Ltd. J.S.B. and J.R. are full-time employees of RxCelerate Ltd. The other authors declare no competing interests.

867 ***Figure Legends***

868 **Figure 1.** Pro-BMP9 and pro-BMP10 are equivalent ALK1-ligands. **a** Dose-dependent signalling
869 assays in PAECs. Serum-starved PAECs were treated with different ligands at 2.48 pM (white
870 bars), 8.27 pM (light grey bars) and 27.3 pM (dark grey bars) (using monomer molecular
871 weight, equivalent to 0.03, 0.1 and 0.33 ng ml^{-1} BMP9 GF-domain concentration) for 1 hour.
872 Changes in the *ID1* gene expression were monitored using RT-qPCR. Data were presented as
873 fold change relative to untreated cells, and means ± SEM of 3 independent experiments are
874 shown. Source data are provided as a Source Data file. **b-d** Volcano plots comparing changes in
875 global gene expression in PAECs after pro-BMP9 or pro-BMP10 treatment. Serum-starved
876 PAECs were treated with 25 pM of pro-BMP9 or pro-BMP10 (purity can be found on SDS-PAGE
877 with silver staining in Supplementary Fig 8a, lanes 1&4) for 1.5 hours before RNA was
878 extracted for microarray analysis. Four different primary PAEC lines were used. Red dots
879 above the dashed line represent the changes in target genes with adjusted *p* values of less than
880 0.05. Several representative target genes are highlighted in **c**&**d**. Full list of genes can be found
881 in Supplementary Data 1 and 2. **e** Affinity measurements of BMP9 and BMP10 for ALK1 using
882 Biacore. A CM5 Biacore chip was immobilised with ALK1 dimer (ALK1-Fc) or monomer (in-
883 house purified ALK1 ECD, purity can be seen in Supplementary Fig 8a, lane 7). The
884 sensorgrams of BMP9, pro-BMP9, BMP10 and pro-BMP10 binding raw data (in black lines)
885 were overlaid with a global fit to a 1:1 model with mass transport limitations (red lines). **f** A
886 summary of kinetic parameters for ligand-receptor interactions derived from the Biacore
887 measurements in **e**.

888

889 **Figure 2.** Crystal structure of human BMP10:ALK1 complex at 2.3 Å. **a** Crystal structure of
890 BMP10 (cyan) in complex with ALK1 (magenta), overlaid with the structure of
891 BMP9:ALK1:ActRIIb complex (PDB:4FAO, in grey and semi-transparent). Mol A and Mol B are

892 the two BMP monomers whose interfaces with ALK1 (Mol C) were analysed in (**b**). **b**
893 Comparison of the buried interface upon complex formation between BMP10:ALK1 and
894 BMP9:ALK1 (from 4FAO). Total buried surface area and the contributing residues were
895 calculated using PDBePISA server.
896
897 **Figure 3.** Specificity determinants in the BMP9 and BMP10 subfamily. **a** Sequence alignment of
898 representative ALK-binding BMPs. GF-domain sequences of ALK1-binding BMP9 and BMP10,
899 ALK6-binding BMP14, ALK3-binding BMP2 and BMP4, as well as ALK2-binding BMP6 and
900 BMP7 are aligned. Lines over and below the sequences highlight the residues at the type I and
901 type II receptor-binding surface based on BMP10:ALK1 and BMP9:ALK1:ActRIIb structures,
902 respectively. * marks the residues that are conserved among at least 6 out of 7 aligned BMPs.
903 Residues preferentially conserved between BMP9 and BMP10 are highlighted, in cyan for those
904 at the type I site (*conserved region 1*), in blue for those at the type II site (*conserved region 2*)
905 and in yellow for those outside receptor binding surface (*conserved region 3*). BMP10 D338 and
906 P366 are also highlighted in cyan because they make conserved interactions with ALK1 in the
907 crystal structure (Fig 4). **b** Residues from conserved regions 1-3 plotted on BMP10 structure
908 and labelled with full length proBMP10 residue numbers. Fifteen residues from conserved
909 regions 1-3 are shown in spheres, coloured accordingly. The first Gly from conserved region 3
910 is not modelled in the crystal structure, and hence not plotted. **c** An overlay of BMP10 (grey)
911 onto the structures of BMP9 (gold, from 4FAO) [9], BMP2 (green, from 2GOO) [31] and BMP7 (cyan,
912 from 1M4U) [61] is shown from the side view (left) and the top view (right). The red arrows
913 indicate the unique insertion in BMP9 and BMP10.
914
915 **Figure 4.** Conserved region 1 and ALK1-specificity determinants**. a** ALK1-binding residues are
916 mapped onto the BMP10 surface (grey), with those conserved across all BMPs in Fig 3**a**

917 coloured in red, those from the BMP9 and BMP10 conserved region 1 in cyan, and other
918 variable residues in yellow. **b** ALK1 (magenta cartoon) binding to BMP10 (surface), with
919 residues interacting with BMP10 shown in sticks. **c-f** Detailed interactions between BMP10 and
920 ALK1. **g** Sequence alignment of four BMP-binding type I receptors, ALK1, ALK2, ALK3 and
921 ALK6, with the four specificity-determining residues in ALK1 highlighted in yellow. Loop 4 and
922 loop 5 are the two loops surrounding the 3_{10} helix (Supplementary Fig 4). **h** Overlaid structures
923 of BMP type I receptors. The structure of ALK1 in the BMP10:ALK1 complex (magenta) is
924 overlaid onto ALK1 in BMP9:ALK1 complex (PBD:4FAO, orange), ALK3 (PDB:2GOO, light green)
925 and ALK6 (PDB:3EVS, light grey). ALK1 residues highlighted in (**g**) are shown in sticks.
926
927 **Figure 5.** Conserved region 2 and type II site analysis. **a** ActRIIb-binding residues (based on
928 PDB:4FAO, ActRIIb in semi-transparent cartoon) are mapped onto BMP9 surface (grey), with
929 those conserved across all BMPs in Figure 3a coloured in red, those from conserved region 2 in
930 blue, and other variable residues in yellow. **b** Type II binding surface of BMP9 (left) and BMP10
931 (right), showing as electrostatic surface (generated in PyMOL, red representing negatively
932 charged and blue positively charged surface). ActRIIb is shown in orange, semi-transparent
933 cartoon. **c** Residues from BMP9 conserved region 2 make three backbone β-sheet and one
934 sidechain H-bond interactions with ENG (PDB:5HZW, ENG in green, BMP9 in cyan). BMP10 is
935 overlaid onto BMP9 and shown in grey, with 4 conserved region 2 residues shown in blue
936 spheres. Sidechains of other residues are omitted for clarity. **d** Sequence alignment of human
937 BMP10 prodomain (hBMP10_pro) with mouse BMP9 prodomain (mBMP9_pro) and human
938 BMP9 prodomain (hBMP9_pro). Residues at the BMP9-binding surface are highlighted in
939 yellow and those that make direct interactions with BMP9 GF-domain are marked with *.
940 Residues that make main chain interactions are also marked with ^. Only the prodomain
941 regions that interact with BMP9 GF-domain are shown, and full-length alignment of

hBMP9_pro and hBMP10_pro can be found in Supplementary Fig 5. **e** Residues in conserved region 2 of BMP9 make four backbone H-bond β-sheet interactions with prodomain (PDB:4YCG; prodomain in orange, BMP9 in cyan. BMP10 is overlaid on BMP9 and shown in grey. 4 conserved BMP10 residues are in blue spheres).

Figure 6. ALK1 can form a complex with pro-BMP9. **a** Overall structure of the human pro-BMP9:ALK1 complex at 3.3 Å (BMP9 in green, ALK1 in magenta, prodomain in orange) overlaid onto the pro-BMP9 structure (4YCG, grey, semi-transparent). **b** Backbones of the BMP9:ALK1 portion from the pro-BMP9:ALK1 structure (BMP9 in green, ALK1 in magenta) overlaid onto the same region in the BMP9:ALK1:ActRIIb structure (4FAO, grey). **c** Overlay of the two prodomains from the pro-BMP9:ALK1 structure (shown in cartoon and coloured in orange and grey respectively) and that from 4YCG (in ribbon, cyan). **d** In the pro-BMP9:ALK1 structure, the conserved region 2 in BMP9 makes the same four backbone H-bond interactions with the prodomain as shown in Figure 5e. Four residues in the conserved region 2 are shown in blue spheres and labelled with BMP10 numbering. **e-h** Analysis of complex formation by analytical gel filtration. Purified pro-BMP9, pro-BMP9 mixed with ALK1, pro-BMP9 mixed with sENG and sENG were run separately on an S200 10/300 gel filtration column which was pre-equilibrated with 20 mM Tris.HCl, 150 mM NaCl, pH 7.4. ***e*** Gel filtration traces. The arrows indicate the elution volumes of the standards. Numbers 1-6 indicate the 6 peaks which were analysed by SDS-PAGE. **f** Middle fraction from each peak was run on an SDS-PAGE. Identities of the proteins on the SDS-PAGE are indicated using colored circles. **g** Consecutive fractions from each gel filtration experiment were run on a non-reducing SDS-PAGE and immunoblotted using an anti-BMP9 prodomain antibody. Each analytical sample run was repeated at least one more time with fraction checked on SDS-PAGE to ensure reproducibility. **h** Cartoon diagrams, using the same coloring scheme as the circles in (**f**), to illustrate that mixing pro-BMP9 with ALK1 leads

to the formation of pro-BMP9:ALK1 complex, whereas mixing pro-BMP9 with sENG leads to the displacement of the prodomain which can be readily detected as a different peak in the gel filtration.

Figure 7. CV2 does not inhibit BMP9 signalling. **a** Structural analysis. BMP10 (grey, with conserved region 2 residues in blue spheres) was overlaid onto the BMP2:CV2 structure (PDB:3BK3, CV2 in magenta and BMP2 in green). Four mainchain H-bonds that stabilise the BMP2:CV2 β-sheet interaction are shown. BMP9 has the same conformation as BMP10 in this region. **b&c** CV2 does not inhibit BMP9 signalling in PAECs. Serum-starved PAECs were treated with BMP9 or pro-BMP9 (at 1 ng ml^{-1} GF-domain concentration) without or with CV2 at 10-, 20-, 50- or 250-fold molar excess for 15 minutes to assess Smad1/5 phosphorylation using immunoblots (**b**) or for 1 hour to assess *ID1* gene expression using qPCR (**c**). One representative of three independent experiments is shown in (**b**). Band intensity was quantified using Image J (version 1.51s). **d** CV2 inhibits BMP4 signalling in PASMCs. Serum-starved PASMCs were treated with BMP4 (25 ng ml^{-1}) without or with CV2 at indicated molar excess for 15 minutes. Immunoblots and quantification were carried out as above. N=3 independent experiments and one representative blot is shown. **e** CV2 inhibits BMP2 but not BMP9 signalling in C2C12 cells. Serum-starved C2C12 cells were treated with BMP2 (130 ng ml^{-1}) or BMP9 (25 ng ml^{-1}) without or with CV2 at the indicated molar excess for 68 hours. ALP activity in the cell lysate were analysed (see Methods). N=7 independent experiments. For all panels, means ± SEM are shown. For **d** & **e**, One-way ANOVA for each BMP treatment group, Dunnett's post hoc analysis against BMP alone-treated controls. Source data are provided as a Source Data file.

Figure 8. Modifying BMP9 signalling specificity by mutagenesis**.** A panel of BMP9 mutants were generated, and tested *in vitro* and *in vivo* as described in the Methods. **a** Mutant proteins were subject to endothelial cell signalling assays (at 0.3 ng ml^{-1} GF-domain concentration) using induction of *ID1* gene expression in hPAECs as a readout, and osteogenic signalling assays (at 10 ng ml^{-1} GF-domain concentration) using ALP induction in C2C12 cells as a readout. Data were normalised to WT BMP9 and shown as fold change relative to WT upon mutation. Each treatment condition was repeated in 3 to 7 independent experiments alongside untreated and WT controls. The exact N number for each condition is given under the column. Means ± SEM are shown. **b** Recombinant WT pro-BMP9, pro-BMP9 D366E, pro-BMP10, as well as BMP2 GF-domain were subject to *in vivo* heterotopic bone-forming assays in the presence and absence of cardiotoxin. Each data point represents the HO result from an independent injection in one leg. N number for each treatment condition is given under each column. Data are presented as % ossification volume relative to the average of BMP2-treated controls. Means ± SEM are shown. **c** Representative CT images (left) and histological staining (right) of *in vivo* formed heterotopic bones after stimulation of indicated BMP molecules in the presence and absence of cardiotoxin. B: osteoid matrix; M: muscle cells. Scale bar = 500 μm.

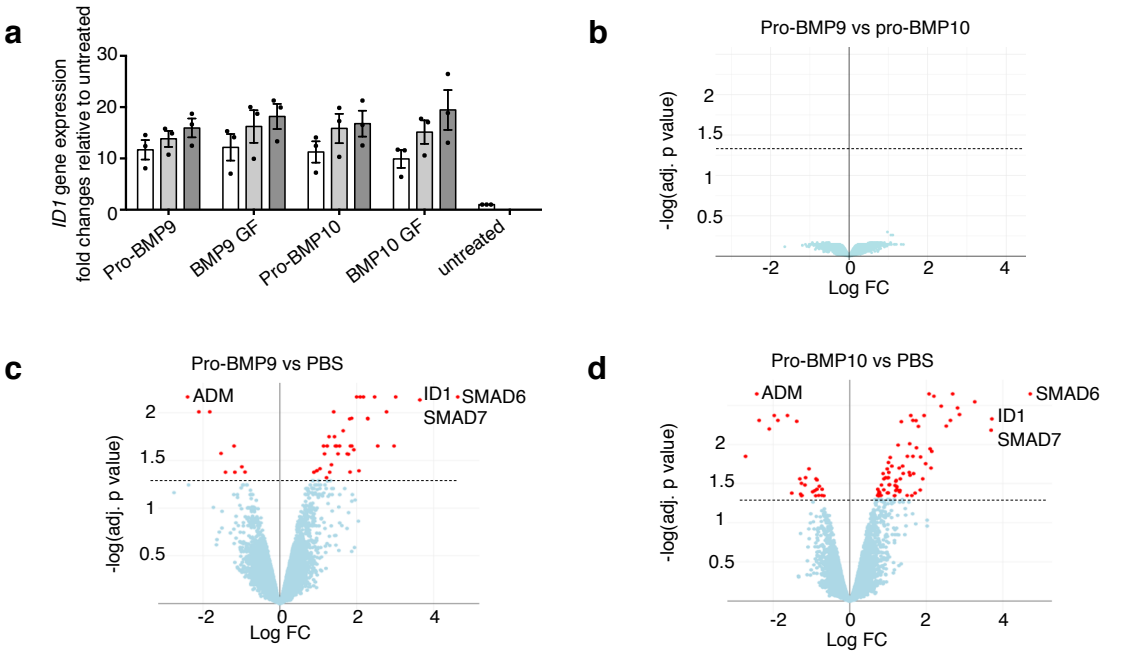

e

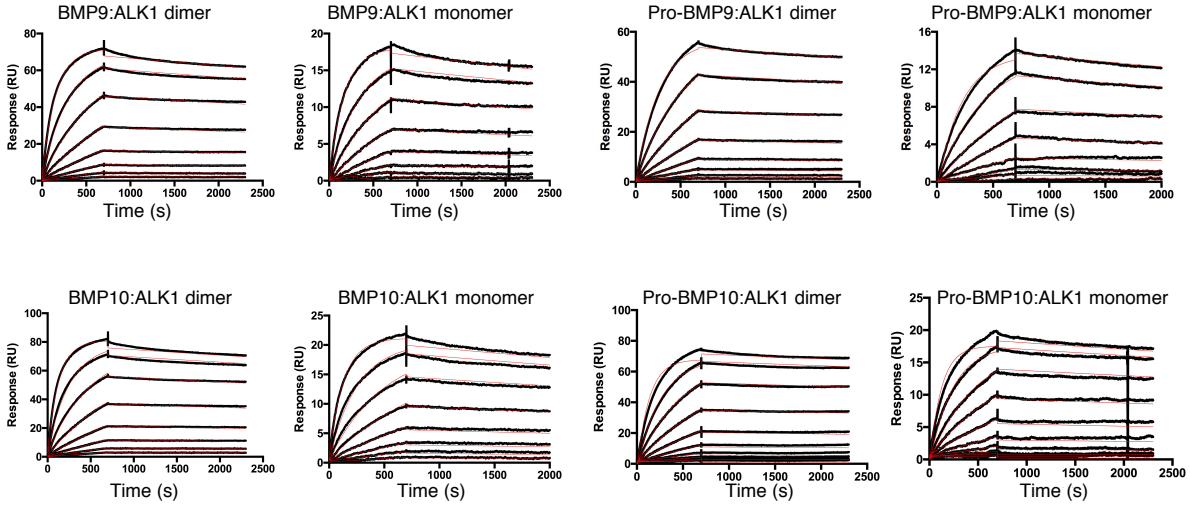

f

	ALK1-Fc (dimer)			ALK1 ECD (monomer)		
	k_a ($M^{-1}s^{-1}$)	k_d (s^{-1})	K_D (pM)	k_a ($M^{-1}s^{-1}$)	k_d (s^{-1})	K_D (pM)
BMP9	1.29×10^6	6.19×10^{-5}	48.1	1.17×10^6	8.37×10^{-5}	71.6
Pro-BMP9	7.91×10^5	4.84×10^{-5}	61.2	9.10×10^5	8.46×10^{-5}	92.9
BMP10	1.54×10^6	5.31×10^{-5}	34.3	1.53×10^6	8.50×10^{-5}	55.7
Pro-BMP10	3.07×10^6	3.44×10^{-5}	11.2	3.32×10^6	5.63×10^{-5}	17.0

a

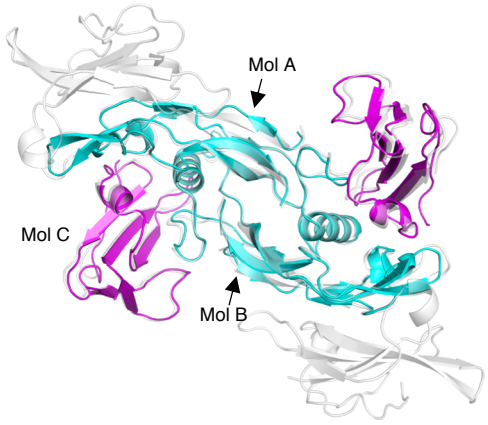

b

	Buried Surface on ALK1 (Mol C)			Buried Surface on BMP		
	Total (Å^2)	% contribution from BMP Mol A	% contribution from BMP Mol B	Total (Å^2)	% contribution from BMP Mol A	% contribution from BMP Mol B
BMP10:ALK1	1072.2	37.0	63.0	1025.5	32.5	67.5
BMP9:ALK1	1193	34.6	65.4	1121.4	30.9	69.1

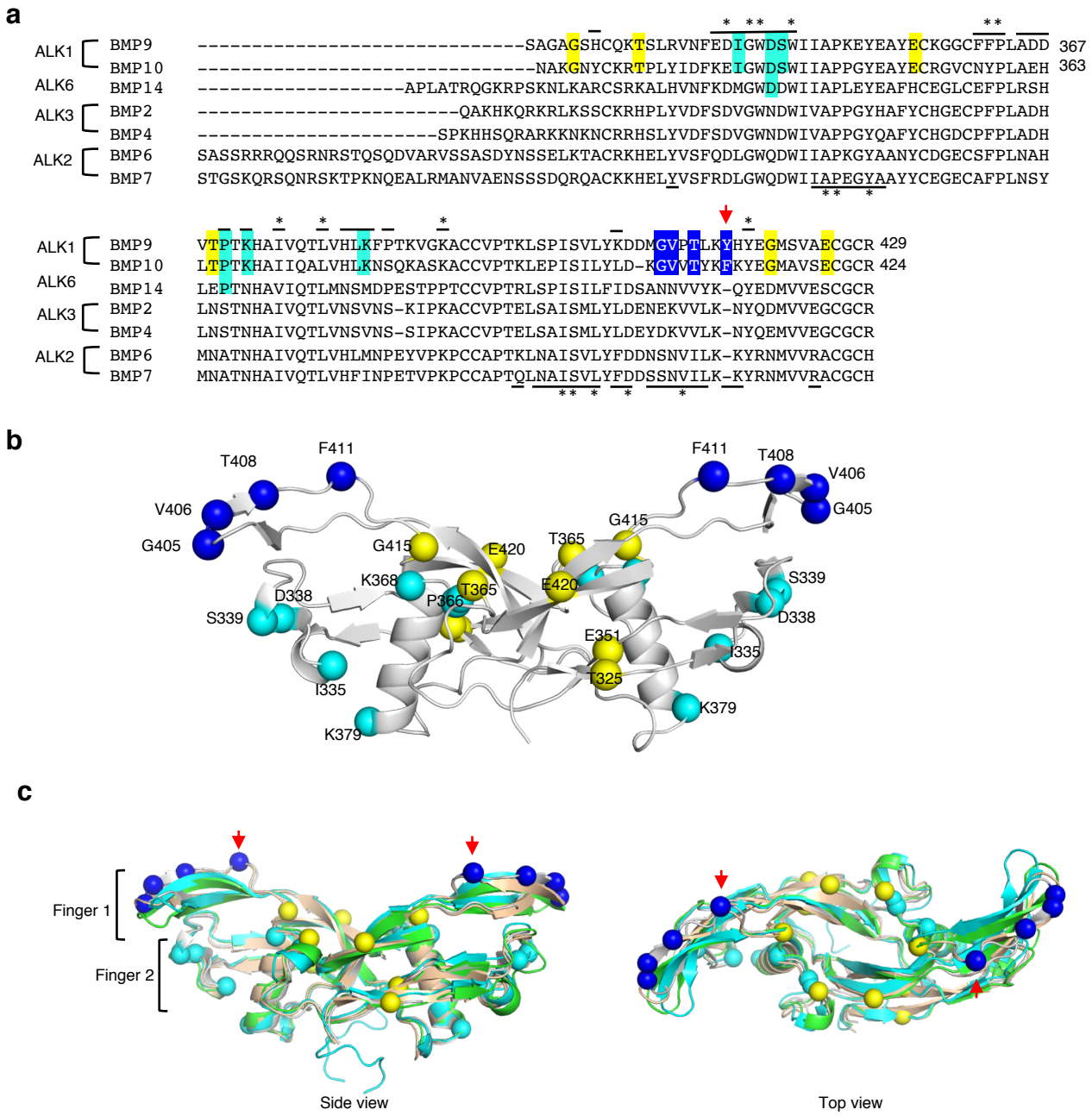
a
ALK1
BMP9
BMP10
ALK6
BMP14
ALK3
BMP2
BMP4
ALK2
BMP6
BMP7
367
363
429
424
b
T408
F411
V406
G405
G415
E420
T365
K368
P366
D338
S339
I335
K379
E351
T325
c
Finger 1
Finger 2
Side view
Top view

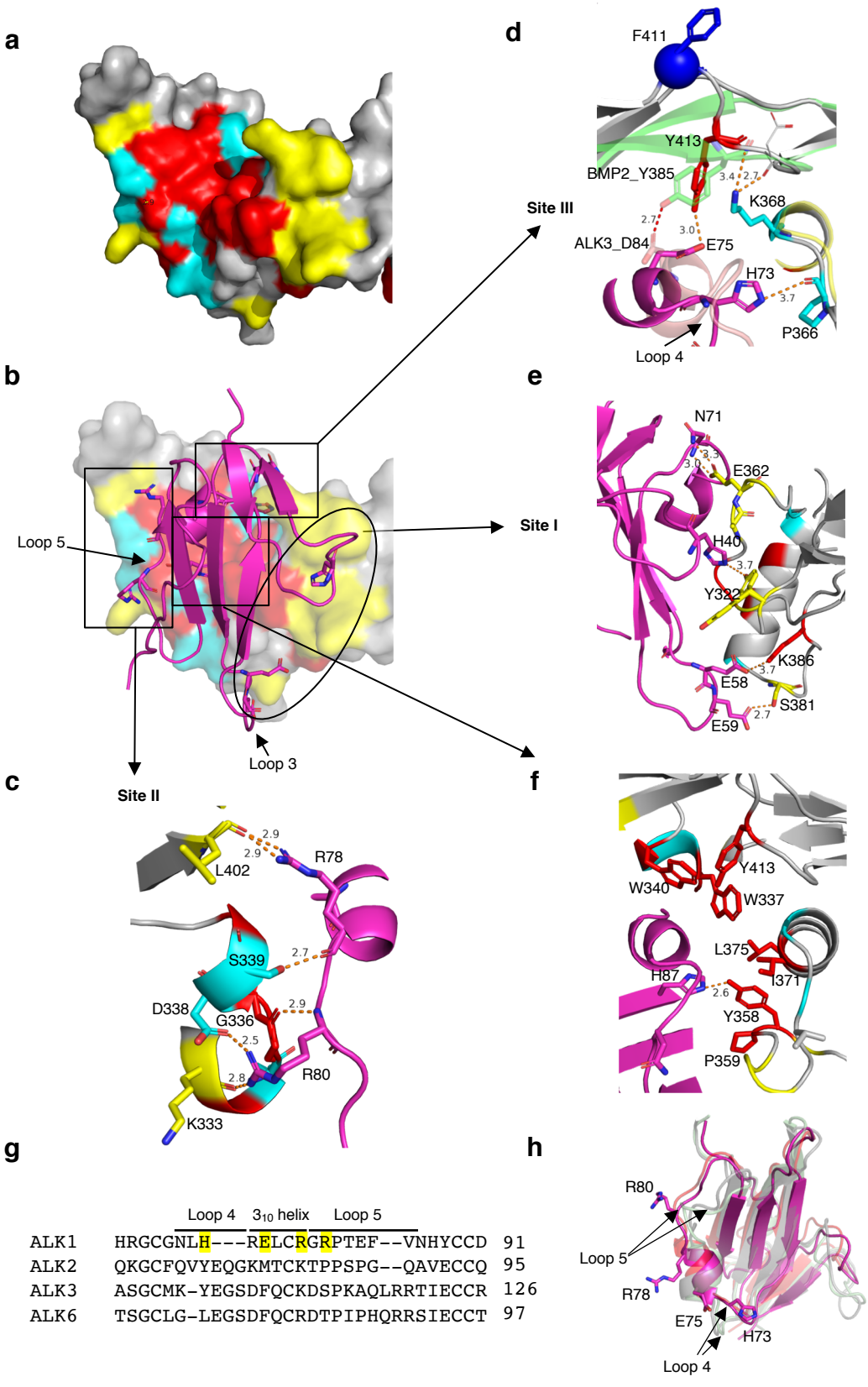
a
b
c
d
e
f
g
h
Loop 5
Loop 3
Site I
Site II
Site III
F411
Y413
BMP2_Y385
K368
ALK3_D84
E75
H73
P366
Loop 4
N71
E362
H40
Y332
K386
E58
S381
E59
L402
R78
S339
D338
G336
R80
K333
W340
W337
L375
H87
I371
Y358
P359
Loop 4 3$_{10}$ helix Loop 5
ALK1 HRGCGNLH---RELCRGRPTEF--VNHYCCD 91
ALK2 QKGCFQVYEQGKMTCKTPPSPG--QAVECCQ 95
ALK3 ASGCMK-YEGSDFQCKDSPKAQLRRTIECCR 126
ALK6 TSGCLG-LEGSDFQCRDTPIPHQRRSIECCT 97

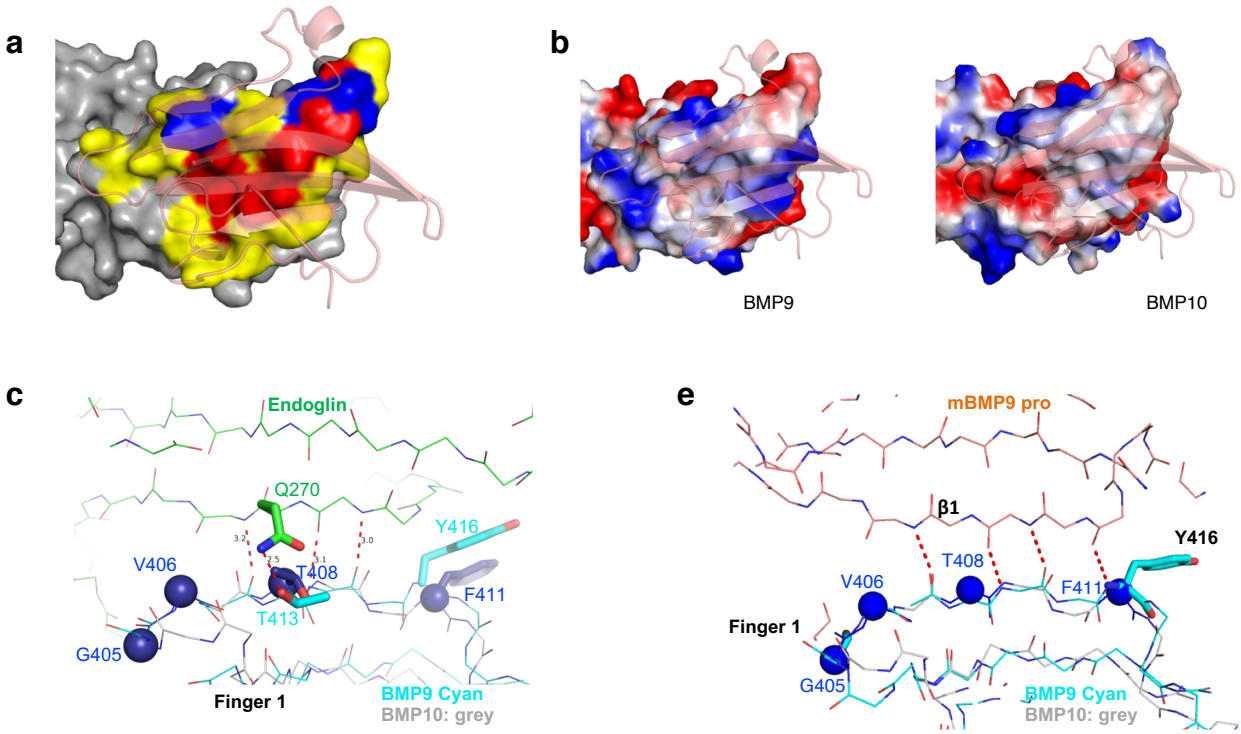

d

```
                                  α2                  β1
hBMP10_pro    78 KVDPPEYMLELYNKFATDRTSMPSANIIRSFKNEDLFSQPVS-FNGLRKYPLLFNVSIPH  126
mBMP9_pro        RAEPPQYMIDLYNRYTTDKSSTPASNIVRSFSVEDAISTAATEDFPFQKHILIFNISIPR
hBMP9_pro     82 RVEPPQYMIDLYNRYTSDKSTTPASNIVRSFSMEDAISITATEDFPFQKHILLFNISIPR  131
                  *     *     *     *  * *
                        ^           ^ ^ ^

                                  α5
hBMP10_pro   254 IVFSDDQSS-DKERKEELNEMISHEQLPELDNLGLDSFSSGPGEEALLQMRSNIIYDST-  311
mBMP9_pro        VVFSNDRSNGTKETRLELKEMIGHEQETMLVKTAKNAYQVAGESQEEEGLDGYTAVGPLL
hBMP9_pro    255 VVFSNDHSSGTKETRLELREMISHEQESVLKKLSKDGSTEAGESSHEEDTDGHVAAGSTL  314
                        *   *   *   ** *
```

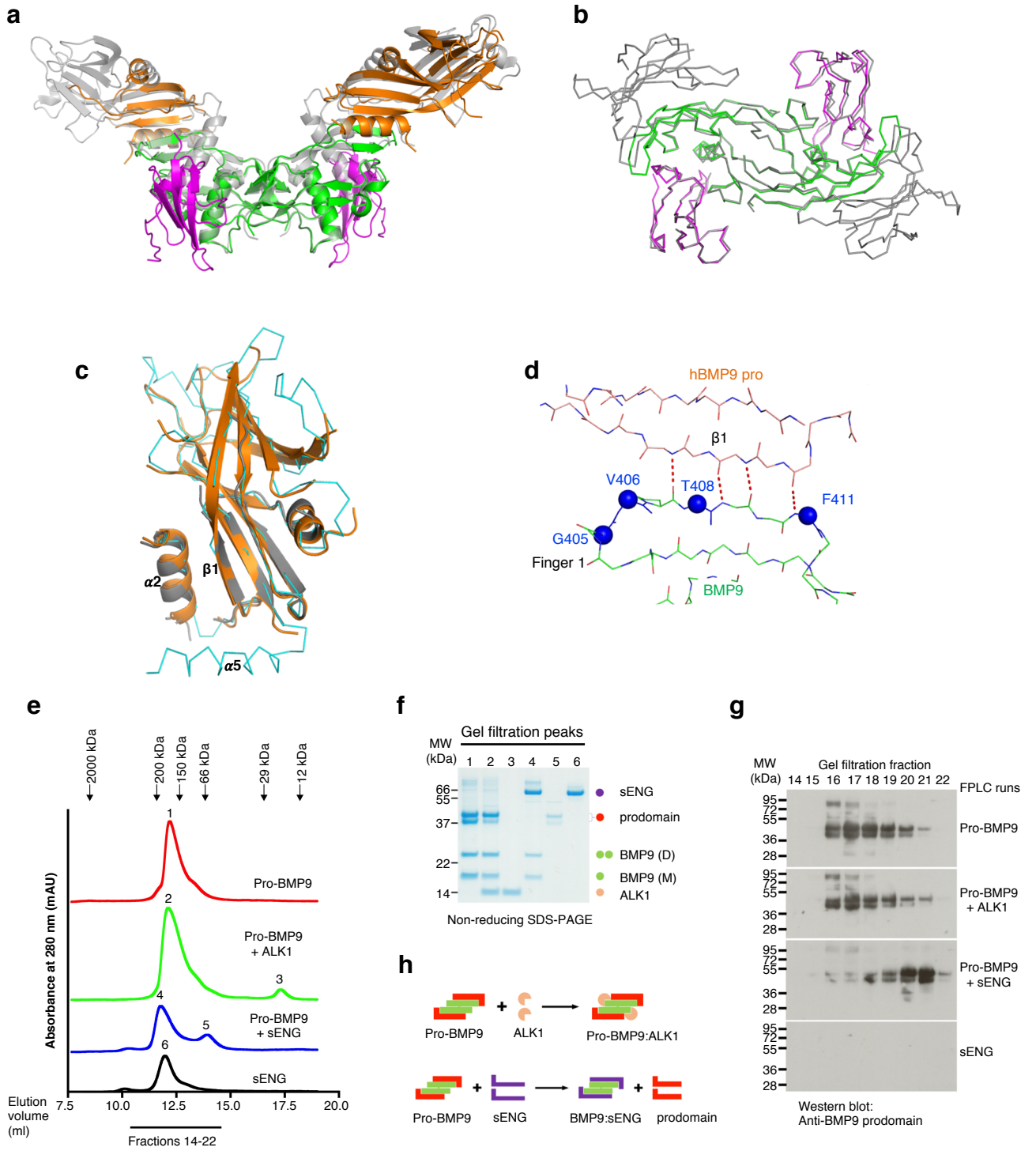
a
b
c
α2
β1
α5
d
hBMP9 pro
β1
V406
T408
F411
G405
Finger 1
BMP9
e
2000 kDa
200 kDa
150 kDa
66 kDa
29 kDa
12 kDa
Absorbance at 280 nm (mAU)
Pro-BMP9
Pro-BMP9 + ALK1
Pro-BMP9 + sENG
sENG
Elution volume (ml)
7.5
10.0
12.5
15.0
17.5
20.0
Fractions 14-22
f
Gel filtration peaks
MW (kDa)
1 2 3 4 5 6
66
55
37
22
14
sENG
prodomain
BMP9 (D)
BMP9 (M)
ALK1
Non-reducing SDS-PAGE
h
Pro-BMP9
ALK1
Pro-BMP9:ALK1
Pro-BMP9
sENG
BMP9:sENG
prodomain
g
MW (kDa)
Gel filtration fraction
14 15 16 17 18 19 20 21 22
FPLC runs
Pro-BMP9
Pro-BMP9 + ALK1
Pro-BMP9 + sENG
sENG
Western blot:
Anti-BMP9 prodomain

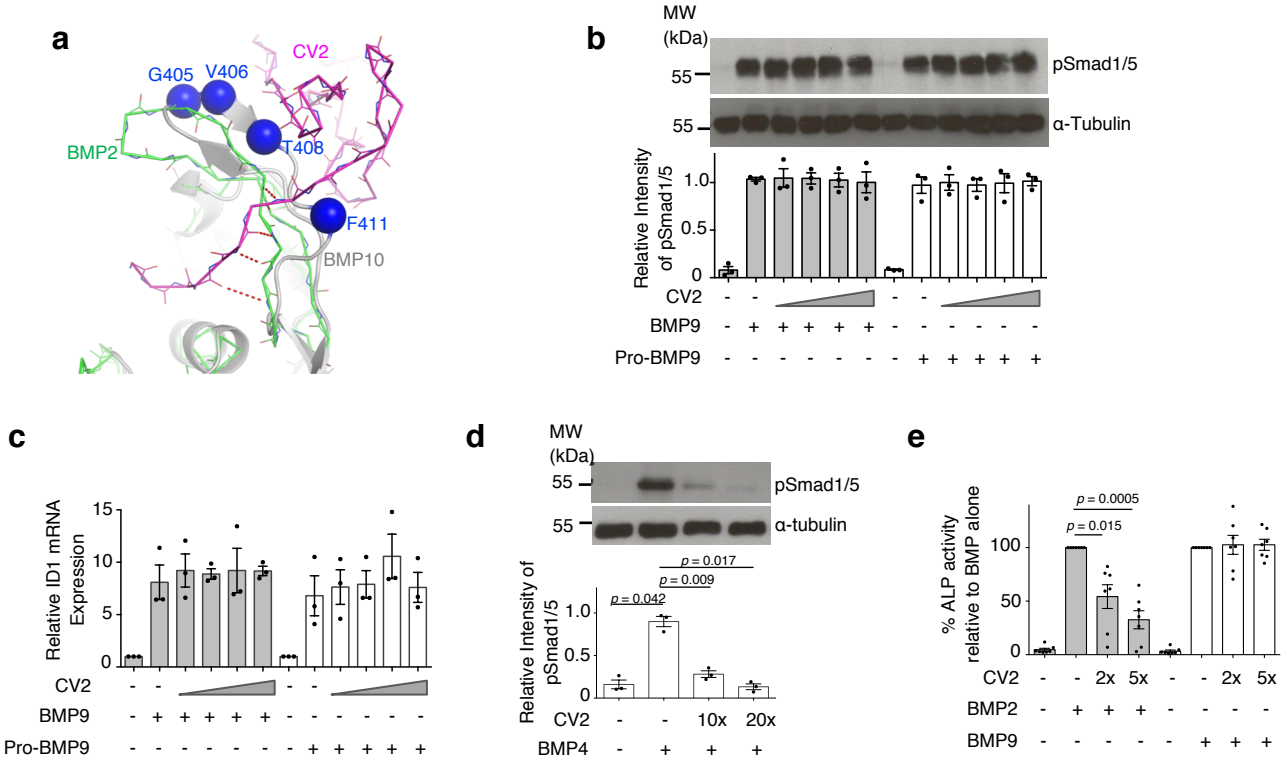
a
G405
V406
CV2
BMP2
T408
F411
BMP10
b
MW
(kDa)
55
pSmad1/5
55
α-Tubulin
Relative Intensity
of pSmad1/5
1.0
0.5
0
CV2
BMP9
Pro-BMP9
c
Relative ID1 mRNA
Expression
15
10
5
0
CV2
BMP9
Pro-BMP9
d
MW
(kDa)
55
pSmad1/5
55
α-tubulin
p = 0.017
p = 0.009
p = 0.042
Relative Intensity of
pSmad1/5
1.0
0.5
0
CV2
10x
20x
BMP4
e
p = 0.0005
p = 0.015
% ALP activity
relative to BMP alone
100
50
0
CV2
2x
5x
BMP2
BMP9

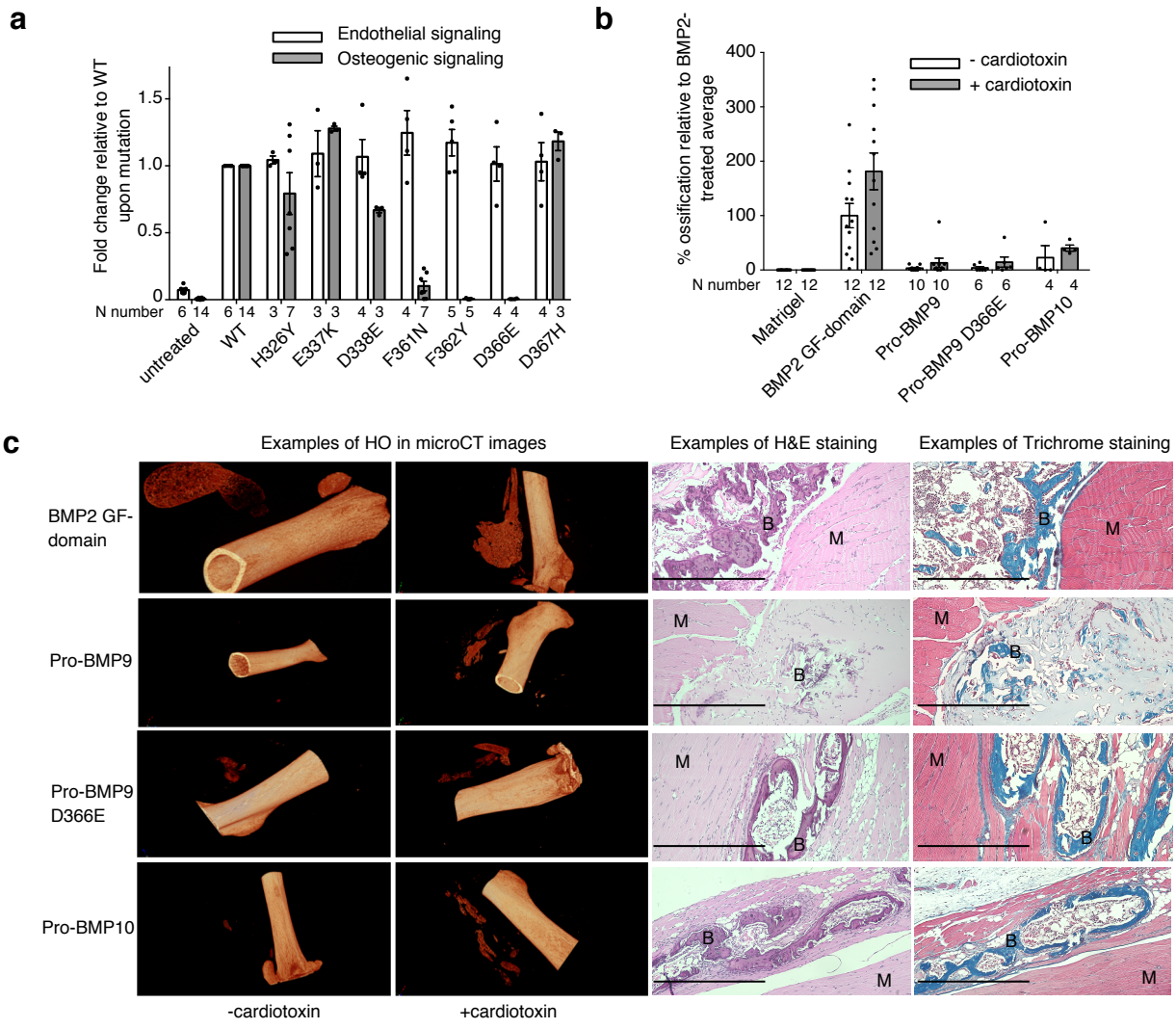
a
Endothelial signaling
Osteogenic signaling
Fold change relative to WT upon mutation
1.5
1.0
0.5
0
N number 6 14 6 14 3 7 3 3 4 3 4 7 5 5 4 4 4 3
untreated
WT
H326Y
E337K
D338E
F361N
F362Y
D366E
D367H
b
% ossification relative to BMP2-treated average
400
300
200
100
0
- cardiotoxin
+ cardiotoxin
N number 12 12 12 12 10 10 6 6 4 4
Matrigel
BMP2 GF-domain
Pro-BMP9
Pro-BMP9 D366E
Pro-BMP10
c
Examples of HO in microCT images
Examples of H&E staining
Examples of Trichrome staining
BMP2 GF-domain
Pro-BMP9
Pro-BMP9 D366E
Pro-BMP10
B
M
-cardiotoxin
+cardiotoxin